Economic Geology, v. 112, pp. 889–918

Physical and Chemical Evolution of the Dabaoshan Porphyry Mo Deposit, South China: Insights from Fluid Inclusions, Cathodoluminescence, and Trace Elements in Quartz*

Wei Mao,[1,2,3,†] Brian Rusk,[2] Fuchu Yang,[4] and Mingji Zhang[1,3]

[1] *State Key Laboratory of Ore Deposit Geochemistry, Institute of Geochemistry, Chinese Academy of Sciences, Guiyang, Guizhou 550081, China*

[2] *Department of Geology, Western Washington University, Bellingham, Washington 98225*

[3] *University of Chinese Academy of Sciences, Beijing 100049, China*

[4] *Guangdong Dabaoshan Mining Company Limited, Shaoguan, Guangdong 512100, China*

Abstract

The Dabaoshan polymetallic deposits in the Nanling Range, South China, consist of porphyry and skarn-type Mo mineralization genetically related to Jurassic porphyritic intrusions and adjacent strata-bound Cu-Pb-Zn mineralization hosted in mid-Devonian limestone. Porphyry Mo mineralization is characterized by the superposition of multiple generations of crosscutting quartz-bearing veins including: barren quartz veins (V1), quartz-molybdenite veins with K-feldspar alteration halos that host the bulk of the Mo mineralization (V2), quartz-pyrite veins with muscovite alteration (V3), and late base metal mineralization with argillic alteration (V4), as well as limestone-hosted strata-bound Cu-Pb-Zn mineralization (VS). Fluid inclusion petrography and microthermometry combined with cathodoluminescent textures and trace elements in quartz reveal changes in pressure and temperature of the hydrothermal system that formed the deposit.

V1 and V2 veins are dominated by low-salinity (1–6 wt % NaCl equiv), CO_2-bearing (4–10 mol %) two-phase inclusions with about 35 vol % bubble trapped in the one-phase field above the solvus of the fluid. V1 veins are dominated by CL-bright granular quartz mosaics with higher CL intensity than any other vein type. This quartz also contains more Ti than any other vein generation (24–89 ppm), while Al, Ge, and Li concentrations overlap with other vein generations. Molybdenum ore-hosting V2 veins are also dominated by CL-bright granular quartz mosaics, but V2 veins display slightly less CL intensity and correspondingly lower Ti concentrations (10–65 ppm). V3 veins have a broader spatial distribution than V1 and V2 veins, extending from inside the porphyries out into the adjacent limestone. These veins are also dominated by low-salinity (2–6 wt % NaCl equiv), CO_2-bearing (4–7 mol %) two-phase inclusions, these containing about 45 vol % bubble trapped above their solvus. V3 veins are dominated by CL-dark quartz with euhedral growth zones of oscillating CL intensity and systematically lower Ti concentrations than previous vein generations (1.5–12 ppm). Minor V4 veins cut all the above vein generations and also occur as late infill in V3 veins. Low-salinity (4–7 wt % NaCl equiv), CO_2-bearing (4–5 mol %) two-phase inclusions with about 20 vol % bubble prevail in V4 veins. V4 veins have the lowest CL-intensity quartz of all vein types, with euhedral growth zones of oscillating CL intensity and the lowest Ti concentration of all vein types (0.54–5.3 ppm).

Intersections of fluid inclusion isochores with Ti-in-quartz isopleths indicate that the hydrothermal system evolved from near-magmatic pressures and temperatures of 2.7 ± 0.2 kbars and 650° ± 40°C for V1 veins to 1.9 ± 0.2 kbars and 530° ± 40°C for V2 veins to 0.65 ± 0.2 kbars and 400° ± 40°C for V3 veins. V4 veins, which lack rutile, formed as the system cooled to 250° to 300°C at maximum pressures of 0.40 to 0.65 kbar.

Unlike nearly all other reported porphyry-type ore deposits, quartz-bearing veins from the Dabaoshan porphyry Mo deposit contain few halite-bearing or vapor-dominated fluid inclusions in any vein type. The dearth of such fluid inclusions, coupled with the abundance of two- and three-phase CO_2-bearing low-salinity fluid inclusions in all vein types is evidence that the formation conditions of V1 to V4 veins remained above the V-L surface in the H_2O-NaCl-CO_2 system, such that fluid unmixing rarely occurred in the Dabaoshan hydrothermal system. This is further supported by only rare evidence for quartz dissolution textures in all vein types, implying that pressures were dominantly higher than zone of retrograde quartz solubility. Taken together, the fluid inclusions, CL textures, and quartz trace element data indicate that the Dabaoshan porphyry Mo deposit is one of the deepest formed porphyry-type ore deposits, having formed at depths of 6 to 7 km below surface. The extreme depth and lack of fluid unmixing inhibited Cu precipitation in the porphyry system, and instead allowed Cu to remain in solution to precipitate with Pb and Zn upon interaction with the surrounding Devonian limestone.

Introduction

Porphyry-type ore deposits are characterized by multiple mineralization and alteration events. These can be distinct in time and physiochemical conditions of vein formation, but overlap spatially in a given rock volume (e.g., Hedenquist et al., 1998; Selby et al., 2000; Muntean and Einaudi, 2001; Wilson et al., 2003; Seedorff et al., 2005; Maydagán et al., 2015). The superimposition of successive mineralization events complicates our ability to infer the evolution of the physiochemical conditions of vein formation based on traditional methods such as fluid inclusion microthermometry, isotopes,

† Corresponding author: e-mail, dzmaowei@163.com

* A digital supplement containing electronic Appendixes 1–6 for this paper is available at http://economicgeology.org/ and at http://econgeol.geoscienceworld.org/.

0361-0128/17/4493/889-30

Submitted: January 17, 2016
Accepted: November 24, 2016

or mineral thermodynamic equilibria (e.g., Wilson et al., 2003; Landtwing et al., 2005; Maydagán et al, 2015).

Although most porphyry Cu (Mo-Au) deposits have been suggested to form at depths of 3 to 5 km below the Earth's surface (Hedenquist et al., 1998; Redmond et al., 2004; Seedorff et al., 2005; Klemm et al., 2008; Sillitoe, 2010), the complete extent of the causative hydrothermal systems has greater dimensions than orebodies themselves. Root zones of porphyry systems, where porphyry dikes merge down into porphyritic granite cupolas, exist at depths of up to 10 km (Dilles, 1987; Dilles et al., 2000; Seedorff et al., 2008). Early and deep vein formation in some porphyry-type deposits has been shown to occur at pressures of 2 kbars or higher, corresponding to depths greater than 6 km in a number of districts (e.g., White Pine Fork molybdenum prospect, Utah: John, 1989; Superior district, Arizona: Manske and Paul: 2002; Butte, Montana: Rusk et al., 2008a; Altar, Argentina: Maydagán et al., 2015). Most of these deep-early veins are quartz dominated and lack Cu-Fe sulfides, although molybdenite is present in some of them.

Pressures and depths of ore formation are notoriously difficult to determine and appropriate estimations based on fluid inclusion analysis rely on at least one external constraint of temperature or pressure in order to make isochoric corrections to derive actual trapping temperature and pressure (Bodnar and Vityk, 1994). External constraints typically include sulfur isotopes or mineral geochemical equilibria (e.g., Brimhall, 1977; Linnen and Williams-Jones, 1990; Selby et al., 2000; Rusk et al., 2008a; Maydagán et al, 2015); however, in many deposits, an external constraint on pressure or temperature is either not available, due to lack of appropriate minerals, or the data may be ambiguous due to complex and cryptic overprinting of multiple mineralization events formed under differing pressure-temperature conditions, but utilizing the same fluid-flow pathways (Landtwing et al., 2005; Müller et al., 2010).

As most veins in most porphyry-type deposits contain quartz, the Ti-in-quartz thermobarometer (e.g., Thomas et al., 2010; Huang and Audétat, 2012), when combined with fluid inclusion microthermometry, yields unique pressures and temperatures of vein formation. However, the Ti-in-quartz thermobarometer may be compromised if multiple generations of quartz are present in individual veins, as has been shown to be the case in many porphyry-type ore deposits (Penniston-Dorland, 2001; Rusk and Reed, 2002; Landtwing et al., 2005; Müller et al., 2010). SEM-CL images reveal textures in quartz that are not otherwise obvious (Smith and Stenstrom, 1965; Sippel, 1968), and these textures can be used to discriminate the sequence of formation in complex multigenerational veins and relate specific minerals and fluid inclusion populations to specific quartz generations (Rusk and Reed, 2002; Landtwing et al., 2005; Müller et al., 2010; Götte et al., 2011; Lambrecht and Diamond, 2014; Maydagán et al., 2015). Because Ti has been shown to be the main CL activator in quartz that forms at temperatures above ~350° to 400°C (Götze et al., 2001; Müller et al., 2003; Rusk et al., 2008b; Götze, 2009; Leeman et al., 2012; Rusk, 2012), the variations in CL intensity directly reflect temperature and pressure fluctuations.

In this study, we use the Ti-in-quartz thermobarometer, CL textures, and fluid inclusion microthermometric data, along with geologic relationships and vein crosscutting relationships in order to reconstruct the pressure-temperature time path of vein formation over the life of the hydrothermal system that formed the Dabaoshan porphyry Mo deposit in the Nanling Range, South China. The combination of these techniques yields new insights into the pressure and temperature fluctuations that result in ore deposition, metal distribution, and porphyry ore deposit formation and yields insights into the hydrologic conditions under which the veins formed.

Geologic Setting

The Nanling Range in South China is famous for its extensive Mesozoic granitic magmatism and related mineralization. It contains more than 50% of the world's W reserves and 20% of the world's total Sn reserves (Zhou et al., 2006; Li and Li, 2007; Mao et al., 2008, 2011; Shu et al., 2011; F.Y. Wang et al., 2011; Li et al., 2012; Sun et al., 2012). Although less abundant than W and Sn, there are also several important Mesozoic Cu and Mo deposits, with the Dabaoshan district hosting the largest porphyry-type Mo deposit in the region (L. Wang et al., 2010, 2011; Mao et al., 2013). The porphyry Mo mineralization is genetically related to and hosted in Jurassic granodiorite porphyries in the northern Dabaoshan district (Fig. 1). Skarn-type Mo mineralization is developed in the northwest of the Dabaoshan district where granodiorite intruded Upper Devonian limestone. The mid-Devonian Donggangling limestone hosts a strata-bound Cu-Pb-Zn deposit covered by siderite and gossan mineralization to the east of the Jurassic porphyries. There is still debate as to whether the strata-bound Cu-Pb-Zn deposit is related to Jurassic porphyry-style mineralization (Liu and Zhou, 1985; Huang et al., 1987; Cai and Liu, 1993a; Xu et al., 2008; L. Wang et al., 2011) or whether it is a volcanic-associated massive sulfide deposit formed in a Devonian submarine environment (Ge and Han, 1986; Yang, 1997; Ye et al., 2011, 2014).

Several tectonic models have been proposed to account for the Mesozoic magmatic and metallogenic events in the Nanling region. These models include asthenospheric upwelling during intraplate lithospheric extension (Hsü et al., 1990; Gilder et al., 1996; Wang et al., 2003, 2004; Chen et al., 2008; Liu et al., 2012) and subduction-related magmatism associated with Pacific plate subduction beneath the active continental margin (Zhou and Li, 2000; Zhou et al., 2006; Li and Li, 2007; Sun et al., 2007, 2012; Li et al., 2008; F.Y. Wang et al., 2011; Li et al., 2012). Zhou et al. (2006) proposed that the tectonic regime in South China changed from the early Mesozoic (T_1-T_3) continent-continent collision in the Tethyan orogenic domain to a late Mesozoic (J_2-K_2) extensional setting related to the subduction of the paleo-Pacific oceanic lithosphere. The extensional setting remained in the Cenozoic and led to the formation of small-scale rifts and magmatic activities (Shu et al., 2004). A southwestward-directed subduction model proposed by F.Y. Wang et al. (2011) can feasibly explain the temporal and spatial distribution of large-scale mid-Mesozoic magmatic and metallogenic events. Based on the high oxygen fugacity in zircons and high F/Cl ratios in apatite from the Dabaoshan porphyries, Li et al. (2012) proposed that slab rollback caused asthenospheric upwelling, decomposed phengite, and ultimately generated the Dabaoshan porphyries and molybdenite mineralization.

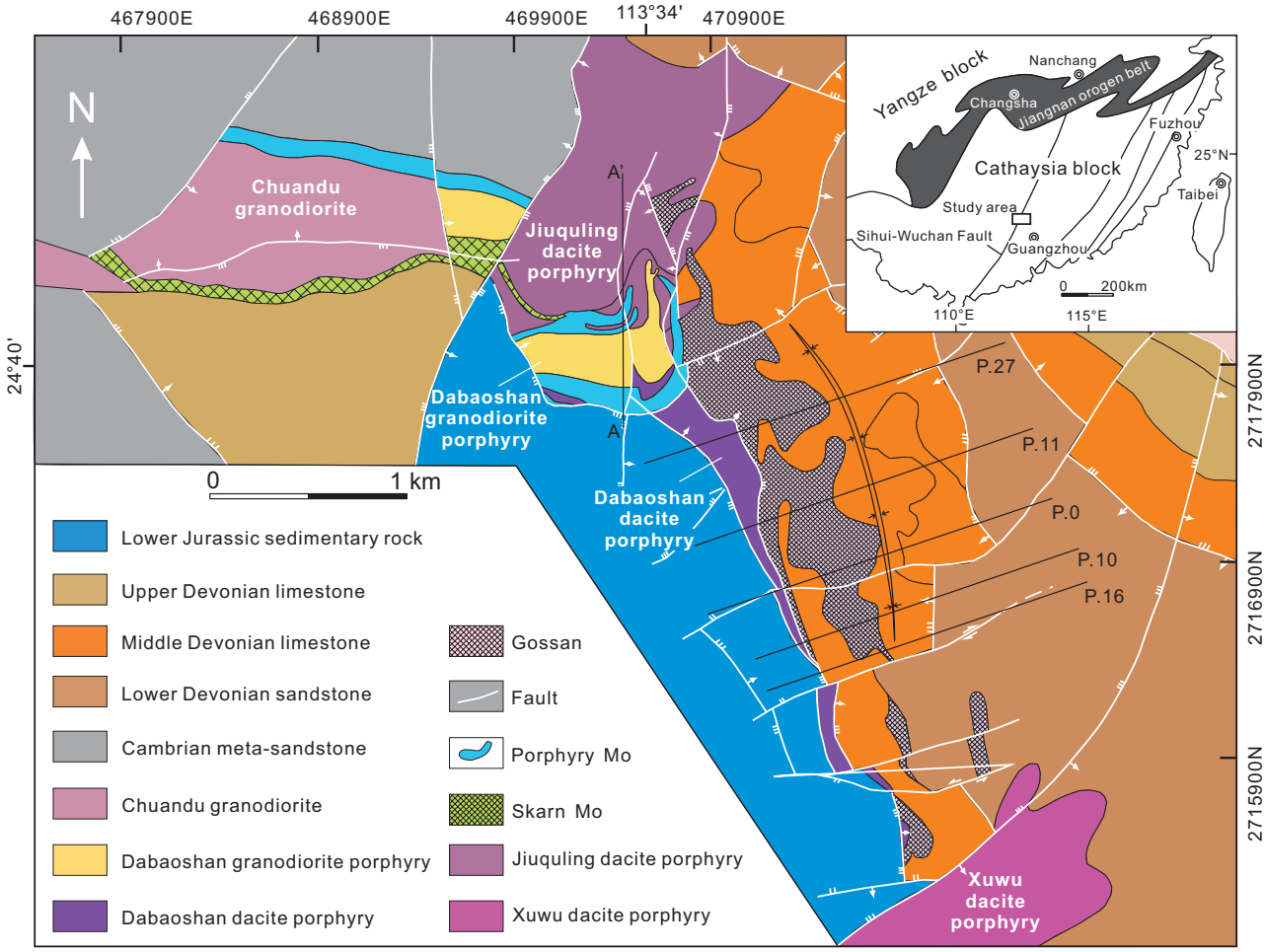

Fig. 1. Geologic map of the Dabaoshan polymetallic deposit, South China (modified after Liu et al., 1985).

The Dabaoshan district lies in the central region of the Nanling Range, where the NE-trending Sihui-Wuchuan fault intersects the E-trending Dadongshan-Guidong tectono-magmatic belt (Fig. 1). The Cambrian Gaotan Formation meta-sandstone is in the northwest part of the district and consists of intercalated graywacke, siltstone, and slate. The Mid-Devonian Donggangling limestone is exposed in the eastern part of the Dabaoshan district and is the dominant host for strata-bound Cu-Pb-Zn mineralization. The Donggangling limestone has been divided into two subformations. The lower subformation consists of carbonaceous mudstone, dolomite, and dolomitic and calcitic sandy shale, and hosts the strata-bound Cu-Pb-Zn mineralization. The upper subformation consists of sandy shale, tuffs, and volcaniclastic breccias that host siderite gangue. The Upper Devonian Tianziling Formation limestone crops out in the west of the district (Fig. 1) and is composed of moderate- to thick-layered micritic limestone intercalated with thin-layered, micritic, silty limestone and massive chert-bearing and dolomitic limestone. It is the main host for Mo skarn mineralization. The Lower Jurassic Jinji Formation is composed of graywackes and shales intercalated with thin marl.

Igneous rocks in the Dabaoshan district include the Silurian Xuwu dacite porphyry, the Jurassic Jiuquling and Dabaoshan dacite porphyries, the Jurassic Dabaoshan granodiorite porphyry, and the Jurassic Chuandu granodiorite (Fig. 1). The Jiuquling dacite porphyry and the Dabaoshan dacite porphyry display porphyritic textures and minor flow structures on their margins, and consist of ~20% plagioclase, ~20% quartz, and ~5% biotite as phenocrysts. The Chuandu granodiorite consists of ~45% plagioclase, ~20% K-feldspar, ~25% quartz, and minor biotite. L. Wang et al. (2011) obtained zircon U-Pb ages of 175.8 ± 1.5 Ma for the Jiuquling dacite porphyry and 175.0 ± 1.7 Ma for the Chuandu granodiorite. Mao et al. (2013) obtained younger zircon U-Pb ages of 162.2 ± 0.7, 160.2 ± 0.9, and 161.0 ± 0.9 Ma for the Jiuquling dacite porphyry, Chuandu granodiorite, and the Dabaoshan granodiorite porphyry, respectively. Despite the age discrepancies between these two studies, the Jurassic intrusions in the Dabaoshan district are considered to have formed at similar times. The Chuandu granodiorite and the Dabaoshan granodiorite porphyry are interpreted to be the same dike that has been offset by a late NNW-striking fault (Fig. 1). The Chuandu granodiorite is 600 to ~700 m more deeply eroded than the Dabaoshan granodiorite porphyry (Chen et al., 2009, unpub. internal rept.). Minor mid-Jurassic diabase dikes cut the porphyries and mineralized rocks. Silurian dacite volcanic rocks in the Jiuquling area have a zircon U-Pb age of 436.4 ± 4.1 Ma (Wu

et al., 2014), generally consistent with the zircon U-Pb age of the Xuwu dacite porphyry (426.9 ± 2.2 Ma; Mao et al., 2013).

Porphyry-type Mo mineralization mostly affected the Jurassic igneous rocks and rarely extends outward into the Jinji Formation or the Donggangling limestone (Figs. 1, 2). Porphyry Mo mineralization is concentrated near the contact between the Dabaoshan granodiorite porphyry and the Jiuquling and Dabaoshan dacite porphyries (Fig. 2). Nine porphyry Mo orebodies have been discovered in the Dabaoshan district, the largest of which is on the eastern side of the Dabaoshan granodiorite porphyry. It plunges 60° to 65° to the east and is ~670 m long at surface with an average Mo grade of ~0.076%. Most of the Mo orebodies consist of quartz-molybdenite stockworks, with vein thicknesses ranging from less than 1 mm to several centimeters. Molybdenite is the dominant ore mineral, along with minor pyrite, scheelite, and bismuthinite. Alteration types change outward and upward from least altered granodiorite porphyry to K-feldspar alteration and then muscovite alteration. Argillic alteration is developed along some late-stage faults (Fig. 2B).

Skarn-type Mo ores are mainly hosted in a garnet skarn zone between the Chuandu granodiorite and the Tianziling limestone (Fig. 1). The garnet skarn zone is ~2,200 m long from east to west, and its thickness varies between 40 and 100 m. The granodiorite is characterized by muscovite alteration near the contact zone, whereas the exoskarn zone is characterized by anhydrite, tremolite, and chlorite. Molybdenite Re-Os dating yielded a mineralization age of 164.0 ± 2.5 Ma (L. Wang et al., 2011; Li et al., 2012), consistent with the age of the porphyries. Together, the porphyry- and skarn-type Mo ores contain 52,000 metric tons (t) Mo metal and 45,000 t WO_3 at average grades of 0.07 and 1.77 wt %, respectively. No economic Cu mineralization has been reported from the porphyry or skarn zones.

A strata-bound Cu-Pb-Zn deposit is situated in the syncline of the lower Donggangling Formation limestone to the east of the Dabaoshan dacite porphyry (Fig. 1). Skarn alteration is developed along the contact zone between the Dabaoshan dacite porphyry and the limestone. Gangue minerals include quartz, muscovite, K-feldspar, biotite, tremolite, epidote, diopside, actinolite, chlorite, and garnet. Ore minerals include chalcopyrite, pyrite, pyrrhotite, galena, sphalerite, and minor arsenopyrite, scheelite, wolframite, hermesite, and bismuthinite. Copper (in chalcopyrite) is dominant in the northern part and Pb-Zn mineralization dominates the southern part of the deposit. The orebodies define strata-bound lenses and are generally consistent with the attitude of the limestone layers. The strata-bound deposit hosts 0.313 Mt of Cu (avg = 0.86 wt %), 20,000 t of Pb (avg = 1.77 wt %), 52,000 t of Zn (avg = 4.44 wt %), and 11 Mt Fe (avg = 48.21 wt %; L. Wang et al., 2011). A 50- to ~60-m gossan overlies the siderite zone in the Donggangling Formation.

Veins and wall-rock alteration

Porphyry Mo-related veins in the Dabaoshan district are classified based on vein and alteration minerals (Table 1, Fig. 3).

Barren quartz veins (V1): Barren quartz veins are the earliest generation of veins and are cut by all other vein types (Fig. 3A, C, D). Some deeper V1 veins have irregular wavy margins, whereas shallower V1 veins have straight walls. V1 veins have a granular internal texture with no internal symmetry. Vein thickness ranges from <1 to about 30 mm. V1 veins are largely

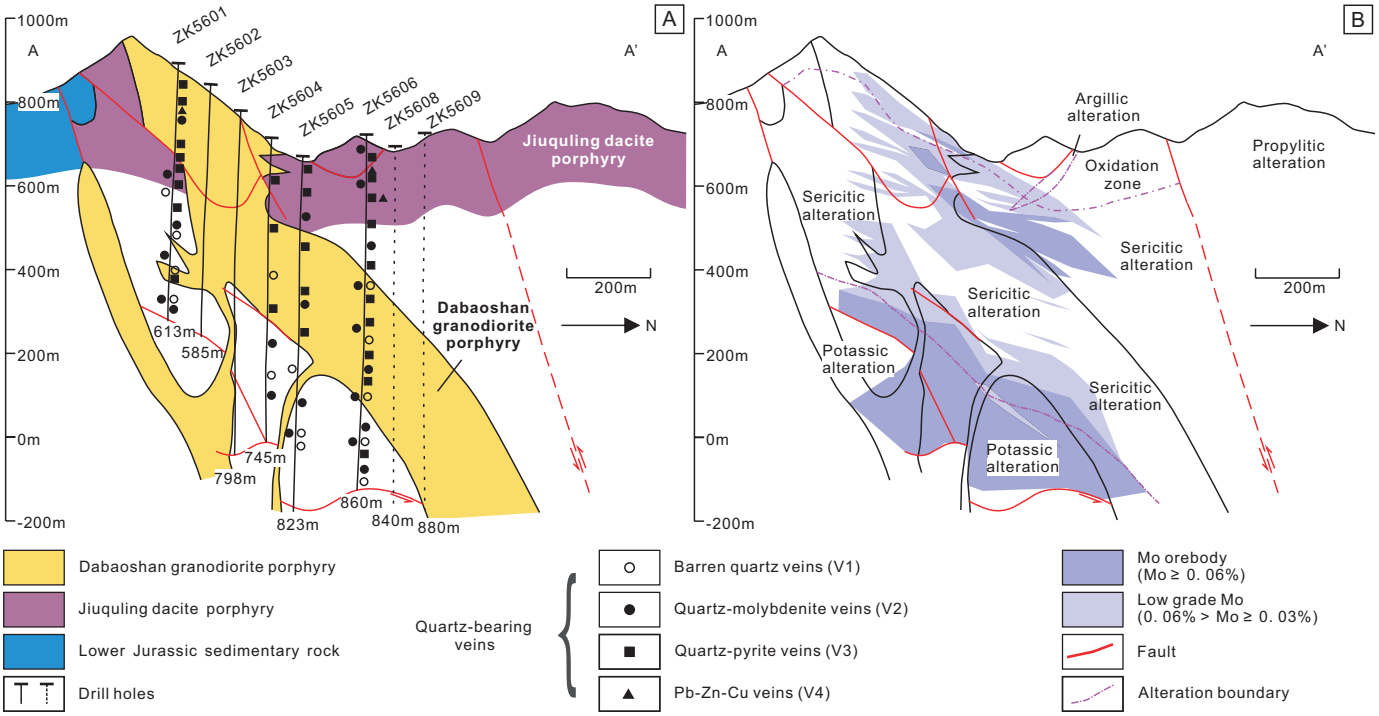

Fig. 2. Geologic map of cross section A-A' of the porphyry Mo deposit at Dabaoshan (modified after unpub. data of the Dabaoshan Mining Company Ltd.). A. The granodiorite porphyry intruded into the early dacite porphyry. Spatial distribution of V1-V4 veins is illustrated in the drill holes. B. Distribution of Mo mineralization and alteration zones.

Table 1. Paragenetic Sequence of Quartz and Calcite Veins and Alteration Minerals Based on Petrography and Crosscutting Relationships

Sample type	Vein minerals	Alteration minerals	Major fluid inclusion types	Vein thickness	Distribution
V1 - Barren quartz veins	qz (rut, mb, py)	kf, bi	B35, DB40	<1 mm to ~ 30 mm	Deep and around the granodiorite porphyry
V2 - Quartz-molybdenite veins	qz, mb (rut, py)	kf, bi, ca	B35, DB40	Several mm to several cm	
V3 - Quartz-pyrite veins	qz, py (cp, gn, sl, bis, rut)	mus, chl, kaol, sp	B45, DB50	<1 mm to over 40 cm	Peripheral and shallow in granodiorite porphyry, dacite porphyry, and Devonian limestone
V4 - Pb-Zn-Cu veins	qz, py, gn, sl, cp, bis	mus, chl, ca, kaol	B20, DB25	Several mm to several cm	Dacite porphyry, Devonian limestone
VS - Strata-bound sulfides	py, cp, gn, sl, qz, bis	chl, act, mus, ca, kaol	B85, DB70		Devonian limestone
VC - Calcite veins	ca	kaol	B5	<1 mm to several cm	Dacite porphyry, Devonian limestone

Mineral abbreviations: act = actinolite, bi = biotite, ca = calcite, cp = chalcopyrite, chl = chlorite, gn = galena, kf = K-feldspar, kaol = kaolinite, mb = molybdenite, py = pyrite, qz = quartz, rut = rutile, mus = muscovite, sl = sphalerite, sp = sphene

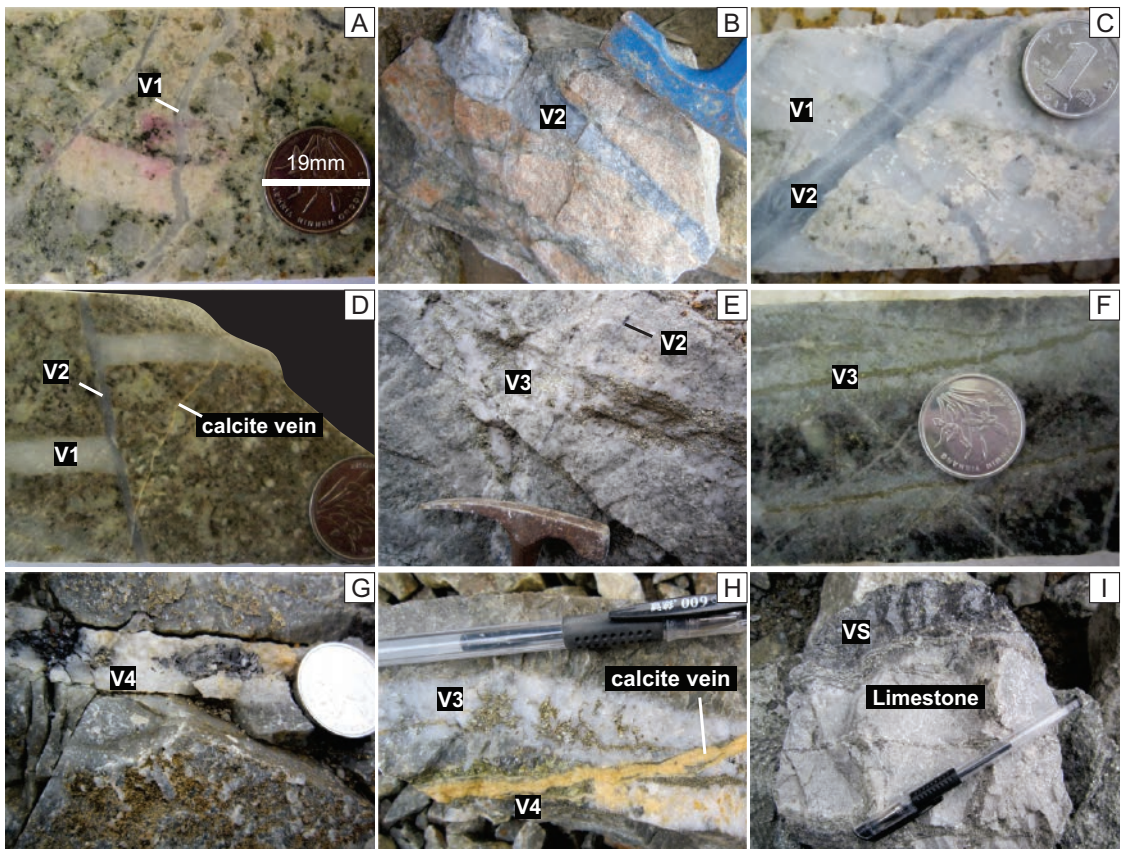

Fig. 3. Veins, mineralization, and alteration in the Dabaoshan polymetallic deposit. A. V1 vein with K-feldspar alteration, hosted in the Jiuquling dacite porphyry. B. V2 vein with K-feldspar alteration, hosted in the Chuandu granodiorite. C. V1 and V2 veins with wavy walls, hosted in the Dabaoshan granodiorite porphyry. D. Calcite vein crosscutting V1 and V2 veins, hosted in the Jiuquling dacite porphyry. E. V3 vein crosscutting V2 vein, hosted in the Jiuquling dacite porphyry. F. Biotite alteration bleached by V3 with muscovite alteration, hosted in the Dabaoshan granodiorite porphyry. G. V4 vein with muscovite alteration. H. V3, V4, and VC veins hosted in the Dabaoshan dacite porphyry. I. Sphalerite, galena, and chalcopyrite mineralization hosted in the Donggangling Formation limestone from the strata-bound deposit.

devoid of sulfides, although minor disseminated molybdenite and pyrite occur in some. Rutile needles and minor anhydrite are typically present. V1 veins have thin K-feldspar alteration halos (<1–5 mm) dominated by K-feldspar with lesser biotite (Fig. 3A). V1 veins are most abundant at depth and are hosted within and around the Dabaoshan granodiorite porphyry, but none is recognized in the adjacent sedimentary rocks (Fig. 2A).

Quartz-molybdenite veins (V2): Quartz-molybdenite veins cut V1 veins (Fig. 3B-D). The V2 vein walls are straight and vein thickness ranges from several millimeters to several centimeters. V2 veins are quartz dominated, with molybdenite as the dominant sulfide, and minor pyrite is present locally. Molybdenite generally occurs as thin platy crystals on the margins of the veins, and/or as central seams. V2 veins contain abundant rutile needles together with minor calcite and anhydrite. Alteration halos are not well developed, but minor biotite and K-feldspar occurs along vein edges. Higher molybdenite content and lower rutile content distinguish V2 veins from V1 veins, although there may be a gradation in molybdenite concentrations from barren quartz veins to quartz-molybdenite veins. V2 veins overlap spatially with V1 veins, but V2 veins extend to shallower depths and, like V1 veins, do not extend into the surrounding sedimentary units (Fig. 2A). Many V2 veins are also observed in the north part of the Dabaoshan dacite porphyry.

Quartz-pyrite veins (V3): Quartz-pyrite veins with fine-grained muscovite alteration (i.e., phyllic or sericitic alteration) are abundant and cut V1 and V2 veins (Fig. 3E, F, H). Vein thicknesses range from <1mm to over 40 cm, and larger V3 veins can be traced over 50 m in length. The spatial distribution of V3 veins is more extensive than V1 and V2 veins, extending from inside the porphyries out to the Donggangling limestone to the east. Pyrite is the dominant sulfide in V3 veins in the porphyries, but some chalcopyrite, galena, sphalerite, and bismuthinite occur in V3 veins in the Donggangling limestone. Quartz makes up over 70 vol % of most V3 veins (Fig. 3E, H) and V3 veins dominated by pyrite that lack quartz are less common (Fig. 3F). Quartz grains in V3 veins typically have euhedral shapes that project toward the vein center. Minor rutile is present in V3 vein quartz. Muscovite alteration halos are 0.1 to 2 cm wide and contain pyrite, quartz, muscovite, and chlorite (Fig. 3E, F, H).

Late Pb-Zn-Cu veins (V4): Late Pb-Zn-Cu veins crosscut V1, V2, and V3 veins. V4 veins also occur as infill in the center of V3 veins (Fig. 3G, H). V4 veins vary from several millimeters to several centimeters in width and have straight walls. Large euhedral quartz crystals project toward the vein center, typically filled with sulfide minerals. Ore minerals include galena, sphalerite, pyrite, chalcopyrite, and minor bismuthinite. Alteration minerals include muscovite and kaolinite. V4 veins are much less common than V3 veins, and most V4 veins occur at shallower depths than the V1, V2, and V3 veins (Fig. 2A).

Strata-bound mineralization (VS): Mineralization in the strata-bound deposit is distinct from the mineralization in the porphyry system. The strata-bound ore varies from massive to semimassive and is locally banded, lamellar, or disseminated. There are also stringer veins (Fig. 3I). Quartz typically makes up less than 15 vol % of the mineralized rocks, which are dominated by chalcopyrite, pyrite, galena, sphalerite, and bismuthinite. Quartz grains are typically several millimeters in diameter or less and are commonly euhedral. Alteration minerals include muscovite, K-feldspar, biotite, tremolite, epidote, diopside, actinolite, chlorite, and garnet.

Calcite veins (VC): Calcite veins are the youngest generation of vein observed in the Dabaoshan district and crosscut all other vein types (Fig. 3D, H). Most of the VC veins are located in the limestone, but some cut veins in the igneous rocks. Calcite veins range in thickness from less than 1 mm to several centimeters and typically have wavy vein walls. Calcite is the main vein mineral and it may be pink or white. VC veins lack sulfides and clearly postdate all of the other vein types.

Methods

Over 400 drill hole samples representing all vein types and alteration assemblages observed at the deposit were collected from 12 drill holes. The drill holes mainly intersect the Dabaoshan granodiorite porphyry, Jiuquling dacite porphyry, and Dabaoshan dacite porphyry and penetrate up to ~1,000 m below surface (Figs. 1, 2). In addition, over 200 hand samples were collected from outcrops.

Fluid inclusion petrography and microthermometry, SEM-CL, and quartz trace element analysis via LA-ICP-MS were carried out on 21 quartz-bearing veins from 18 samples. SEM-CL and transmitted light petrography were used to constrain spots for laser analysis and to relate fluid inclusions to specific generations of quartz in each vein. All analyses were carried out at Western Washington University.

SEM-CL

Color SEM-CL images were acquired on a Tescan Vega3 SEM equipped with a Chroma2 CL detector. An acceleration voltage of 15 kV, a probe current of ~10 nA, and a magnification of 600× was used for most images. Such high magnifications are required by this CL detector, which simultaneously collects SE and BSE images along with color CL images. Due to the small field of view, most images presented here are mosaics of multiple CL images digitally stitched together after acquisition. The colors obtained by CL detector on this instrument are reported to be the actual colors of luminescence and are the same as would be observed through a color CL luminoscope (claimed by the manufacturer, but not specifically tested here). Spots selected for LA-ICP-MS analysis were guided by the combination of CL images and transmitted light images to clearly identify quartz textures and generations, while at the same time minimizing the accidental ablation of fluid and mineral inclusions within the quartz.

LA-ICP-MS

Quantitative LA-ICP-MS trace element analyses were conducted with a NewWave 213-nm Nd: YAG laser system coupled with an Agilent 7500ce ICP-MS. A laser energy density of 15 to 20 J/cm^2, a repetition rate of 10 Hz, and a spot size of 65 to 80 μm were typically used. These conditions resulted in controlled and continuous ablation of quartz, such that spalling or fracturing of quartz was rare. Helium was used as the carrier gas and mixed with argon before entering the torch. The ICP-MS was operated in H mode with an H_2 flow rate of 2 ml/min and oxide production was monitored such that

$^{148}ThO/^{132}Th$ values were always less than 0.2%. Thirty seconds of background signal and 60 s of quartz ablation were collected for each analysis. Twenty-two isotopes were monitored including ^{7}Li, ^{9}Be, ^{11}B, ^{23}Na, ^{27}Al, ^{29}Si, ^{30}Si, ^{31}P, ^{39}K, ^{43}Ca, ^{49}Ti, ^{55}Mn, ^{56}Fe, ^{63}Cu, ^{71}Ga, ^{74}Ge, ^{75}As, ^{88}Sr, ^{118}Sn, ^{121}Sb, ^{137}Ba, and ^{208}Pb. Data were reduced with GLITTER using ^{30}Si as the internal standard assuming stoichiometric quartz. NIST 610 was used as the external standard with element concentrations from Jochum et al. (2011). A natural quartz standard was used as a secondary standard to ensure accurate results for most trace elements of interest (Audétat et al., 2015). Our results on this standard consistently lie within the error range of the preferred values for Li, Ti, and Ge. However, our Al values on the secondary standard were consistently low, suggesting matrix effects between the NIST glass and quartz. We corrected for this discrepancy by normalizing the average measured Al concentrations in the quartz standard to the preferred value and applying the calculated correction factor (typically 10–15%) to all analyses on the samples. The correction factor was determined multiple times throughout an analytical session, every two to three hours, coinciding with bracketing standardization runs used to correct for instrumental drift.

Mineral and fluid inclusions are ubiquitous in most hydrothermal quartz (Flem et al., 2002; Götze et al., 2004; Müller et al., 2012; Rusk, 2012) and the elements contained in those inclusions are considered contamination for our analysis, which is focused on structurally bound trace elements in quartz. Therefore every effort was made to minimize contamination from such inclusions during ablation. Transmitted light was used to find inclusion-free areas, while SEM-CL and BSE images were used to find spots without mineral inclusions or fractures on the surface. However, some contamination from fluid and mineral inclusions is inevitable. All LA-ICP-MS signals were scrutinized closely to filter out all forms of mineral and fluid contamination, by comparing intensity ratios of each element to ^{30}Si, to ensure that the ratio does not change throughout the reduced interval. Where fluid inclusions were ablated, they typically contain Na, K, Mn, Fe, Sr, and Pb in easily detectable quantities. Analysis of many LA-ICP-MS signals show that fluid inclusions rarely contain Li, Al, Ti, or Ge, thus a small amount of contamination from fluid inclusions in these samples will have little effect on these four elements, which are the focus of the results presented here. Some quartz also contains small inclusions of muscovite and/or K-feldspar. Muscovite and K-feldspar inclusions may contaminate Al and K values, but they are not likely to contaminate other elements in the analysis. Potassium and Al were therefore monitored closely in all analyses to identify and avoid such mineral inclusion contamination. Where contamination was present, the analyses were filtered or discarded. All data presented here have been filtered for both fluid and mineral inclusions. We present results from several other elements in quartz in a small percentage of our analyses, only where the optical properties and time-resolved signals are convincing that the elements are not likely caused by accidental ablation of fluid or mineral inclusions.

Nearly 500 spots were analyzed and ~20% of these analyses were discarded due to contamination by fluid and/or mineral inclusions that could not be filtered or avoided during data reduction. Data from 398 spots are presented in Appendices 1 to 6, and 112 of them are labeled with *, indicating that we interpret that the values presented for Mn, Fe, Cu, Ga, As, Sr, Sb, Ba, and Pb are real and unaffected by mineral or fluid inclusions. In all other analyses, we suspect fluid and mineral inclusions may have influenced the concentration of these elements and that the values do not truly represent the concentrations of these elements in quartz.

Fluid inclusion microthermometry

A Linkam fluid inclusion cooling-heating system was used for fluid inclusion microthermometry. The Linkam stage was calibrated at –56.6°C, +0.0°C, and +374.1°C with synthetic fluid inclusions. The precision of temperature measurements on cooling and heating runs are ± 0.1°C and ± 2°C, respectively. A heating rate of less than 0.1°C/s was used for ice-melting temperatures. The heating rate for homogenization temperature measurements was no more than 1°C/s. Heating cycles were used to determine the clathrate-melting temperature in CO_2-bearing inclusions.

Thirteen quartz-bearing veins from 11 samples previously characterized by SEM-CL and ablated for trace elements in quartz by LA-ICP-MS, together with two calcite veins, were analyzed by fluid inclusion thermometry. Fluid inclusion data were acquired on fluid inclusion assemblages (Goldstein and Reynolds, 1994) where inclusions in an assemblage display similar phase proportions and microthermometric behavior, supporting the inference that they were trapped coevally. Homogenization temperatures of each fluid inclusion assemblage lie within a range of 10°C, while ice-melting temperatures lie within a range of 2°C, indicating that the inclusions trapped the same fluid.

The majority of the vapor-liquid inclusions in quartz formed clathrate upon cooling, therefore, the salinities, CO_2 contents, and densities of these inclusions, as well as CO_2-rich inclusions containing vapor CO_2 + liquid CO_2 + aqueous liquid at room temperature, were calculated with the computer program ICE (Bakker, 1997) and the data of Duan et al. (1992a, b). Isochores were calculated for all the inclusions with the computer program ISOC (Bakker, 1997) and the data of Bowers and Helgeson (1983).

Dismemberment of fluid inclusions may lead to changes of fluid composition and/or density (Diamond et al., 2010; Tarantola et al., 2012). Irregular relic fluid inclusions were carefully avoided during microthermometry in order to avoid the impact of postentrapment modification on fluid density (isochores). Hence, the estimation of pressure and temperature conditions is considered to have not been impacted by postentrapment modification.

Results

Color cathodoluminescence textures of quartz-bearing veins

Cathodoluminescence is capable of revealing complicated textures in quartz that are not otherwise obvious (Smith and Stenstrom, 1965; Sippel, 1968). Figure 4 shows at least three distinct types of quartz from a V3 vein. Q1 is defined by growth zones of oscillating CL intensity. Q2 has a bright blue color that has filled fractures. Q3 dark brown to red quartz forms CL-dark patches. These textures are not observable in the corresponding transmitted light image (Fig. 4B).

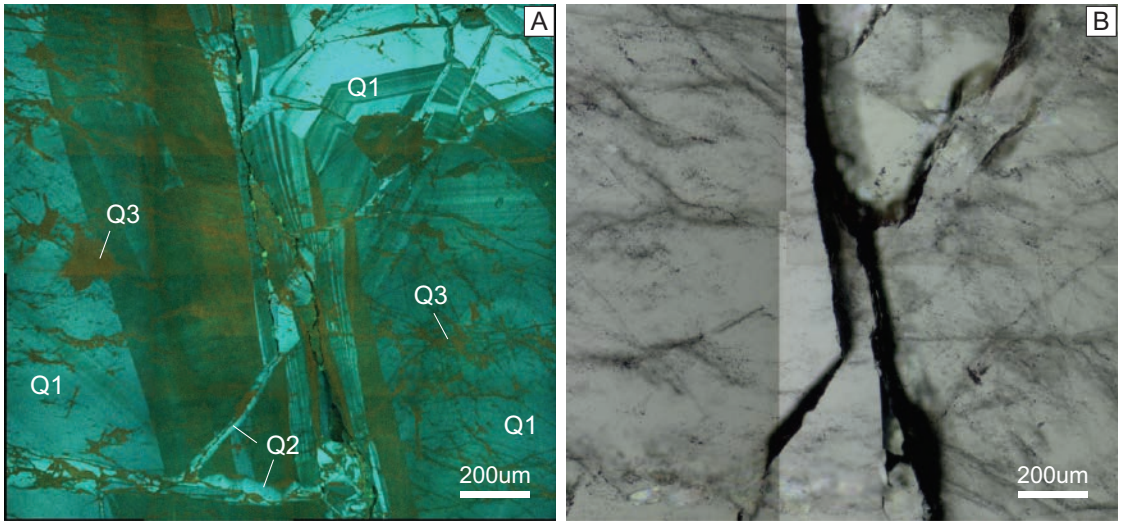

Fig. 4. A. SEM-CL image of quartz from a V3 vein. B. Plane-polarized light image of the same area. At least three types of quartz can be identified in the SEM-CL image, but they are not obvious in the plane-polarized light image.

We obtained CL images of quartz textures from 18 polished thick sections, including multiple samples from each vein generation. Most vein types are characterized by multiple episodes of quartz precipitation, and each vein type is characterized by distinct CL textures that distinguish them from each of the other vein types. Taken together, the textures illustrate the physical and chemical changes in the hydrothermal system during its evolution.

V1 veins (Fig. 5A) are dominated by mosaics of CL-bright blue equigranular quartz grains (V1-Q1; Fig. 5B, C). These quartz grains are higher in CL intensity than quartz in any of the other vein types (Fig. 5B, C). The quartz grains have homogeneous textures and do not display internal growth zonation. In many of the V1 veins, CL bright blue granular quartz has been overprinted by late dark brown to red irregular patches (V1-Q2). These anastomosing fractures and splatters are typically less than 50 μm in thickness.

V2 veins (Fig. 5E) are dominated by mosaics of CL-blue equigranular quartz grains (V2-Q1; Fig. 5D, F) with consistently slightly lower CL intensity than V1-Q1. The quartz grains have homogeneous textures and show no internal growth zonation. In most V2 veins, late dark brown to red irregular patches (V2-Q2) are widely distributed. V2-Q2 patches are typically less than 50 μm in thickness, but become wider where they surround molybdenite and other sulfides. Molybdenite grains are commonly partly surrounded by CL-dark Q2 quartz but are also commonly in contact with CL-bright Q1 quartz (Fig. 5D, F). V2 veins are only distinguishable from V1 veins by a slight decrease in CL intensity. Texturally, the two vein types are similar.

V3 veins (Fig. 6A, B) are dominated by CL-dark blue to red euhedral quartz grains (V3-Q1) with much lower intensity than V1 and V2 quartz. V3 quartz grains show growth zones of oscillating CL intensity and some crystals also display sector zoning (Fig. 7A, B, E). Like V1 and V2 veins, CL-dark brown to red quartz (V3-Q2) is developed in some V3 veins. V3-Q2 either forms the thin, irregular, and discontinuous patches in the V3-Q1 quartz, or is present at boundaries between V3-Q1 grains and sulfides where it tends to be slightly thicker (up to >300 μm; Fig. 7A, B). Some V3 veins contain early CL-bright V1 or V2 quartz that is filled or overgrown by CL-dark zoned V3 quartz. In a few instances, the early bright V1 or V2 quartz appears as rounded cores of V1 or V2 quartz overgrown by CL-dark rims of V3 quartz.

V4 veins (Fig. 6C) are dominated by CL-dark blue euhedral quartz grains with very low CL intensity. In order to produce CL images with visible textures, beam current, contrast and brightness settings were maximized. As in V3 veins, quartz grains in V4 veins show clear growth zones defined by very low CL intensities (Fig. 7C, E). CL-dark brown to red quartz is rare in V4 veins, although some of the sulfides are partly surrounded by late V4-Q2 quartz with extremely low CL intensity (Fig. 7C).

VS veins (Fig. 6D) have quartz grains with very low CL intensities dominated by dark blue to red colors, such that contrast and brightness settings had to be maximized for better demonstration of CL textures (Fig. 7D). VS-Q1 quartz grains display growth zones defined by varying CL intensities and also sector zoning. Similar to V3 veins, VS-Q2 either forms thin, irregular, and discontinuous patches in the VS-Q1 quartz, or is present at boundaries between VS-Q1 grains and sulfides.

Trace elements in quartz-bearing veins

We analyzed 21 trace elements in 21 veins, including all vein types described above. Results from the analysis of 16 elements are given in Appendices 1 to 6. Sodium, K, and Ca may be present, but are not abundant in most quartz (Müller et al., 2003; Götze et al., 2004; Götze, 2009; Audétat et al., 2015), but are common in many mineral and fluid inclusions, thus they were monitored as indicators of contamination from accidental ablation of mineral and fluid inclusions. Quantification of B, P, and Sn can be severely affected by analytical difficulties including polyatomic interferences (Müller et al., 2008; Audétat et al., 2015); therefore, values of these elements were measured, but the quantitative results are not considered reliable and they are not presented. Titanium, Li, Al, and Ge have been shown in numerous previous studies to be common in quartz and to reflect the physical and chemical

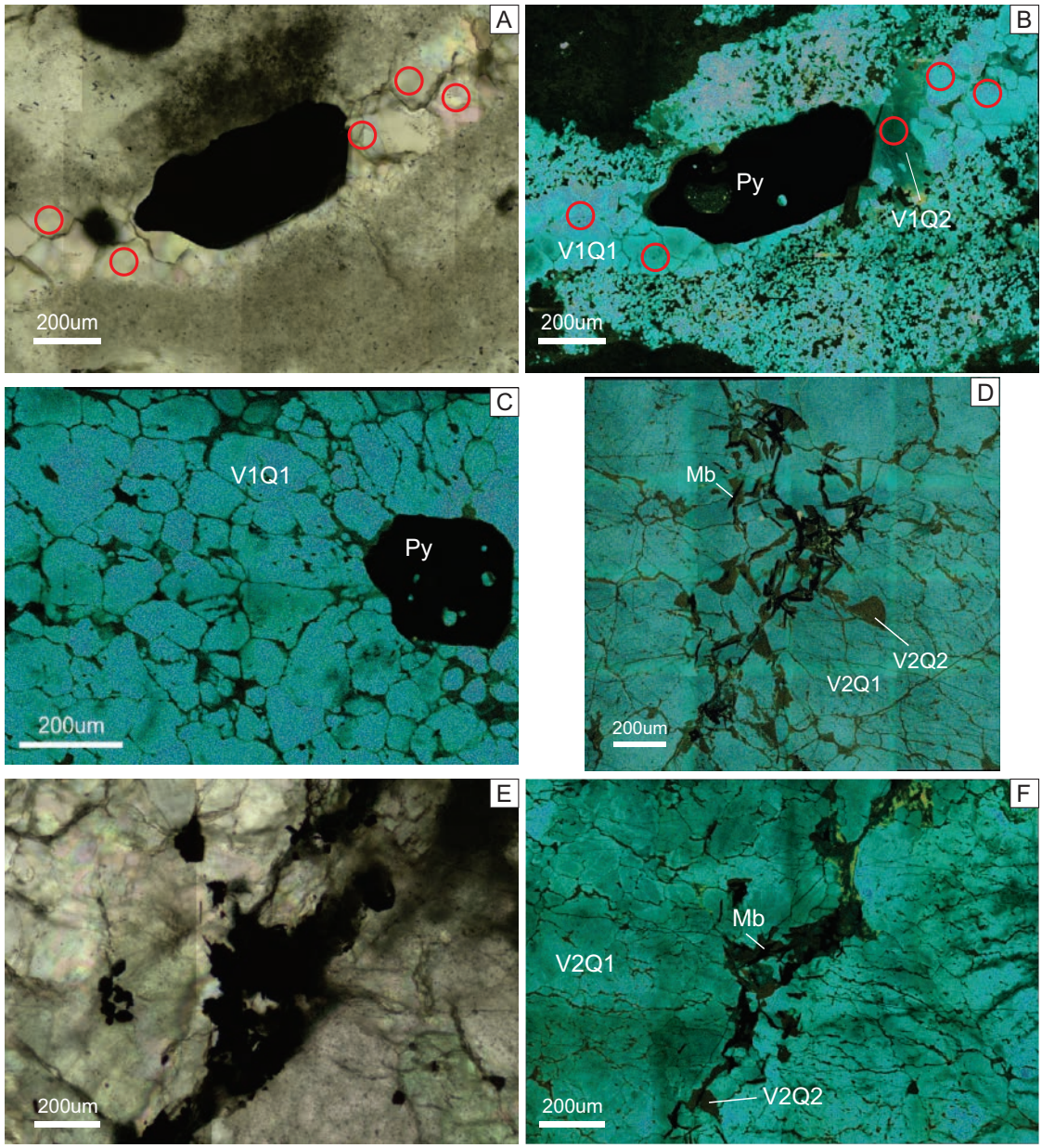

Fig. 5. Transmitted light images and SEM-CL textures of the quartz-bearing veins in Dabaoshan samples. Red circles mark the laser ablation spots of 80-μm diameter. A. Transmitted light image of a V1 vein (5101-11). B. SEM-CL textures in a V1 vein (5101-11), pyrite (Py) is associated with the late dark brown quartz (V1-Q2). C. CL-bright quartz of a V1 vein (5101-12). D) SEM-CL textures in a V2 vein (6204-8). Molybdenite (Mb) is partly surrounded by the late dark brown to red quartz (V2-Q2). E. Transmitted light image of a V2 vein (5601-11). F. SEM-CL textures of a V2 vein (5601-11). Molybdenite (Mb) is partly surrounded by the late dark brown to red quartz (V2-Q2).

conditions of quartz formation (Larsen et al., 2000; Müller et al., 2003, 2012; Götze et al., 2004; Landtwing and Pettke, 2005; Rusk, 2006; Jacamon and Larsen, 2009; Lehmann et al., 2009; Donovan et al., 2011; Götte et al., 2011; Breiter et al., 2013; Audétat et al., 2015). Because these elements are most commonly identified as being structurally hosted by quartz, whereas many of the others mentioned above are vulnerable to contamination from fluid and mineral inclusions, we focus our discussion on these four elements.

Table 2 summarizes the variations of Ti, Li, Al, and Ge concentrations in different generations of quartz veins. Titanium concentrations generally decrease from early to late veins, from 30 to 50 ppm in V1-Q1 to 10 to 20 ppm in V2-Q1, to 3 to 7 ppm in V3-Q1, to 0.5 to 1.5 ppm in V4-Q1 (Fig. 8A). In V3 veins in samples from the Donggangling Formation limestone (DBS13-16 and DBS13-28), Q1 contains slightly less Ti than in Q1 of V3 veins situated in the porphyries (5101-2, 5101-3, and DBS13-47; Fig. 8). Average Li concentrations increase through time, from 0.38 ppm in V1-Q1 to 0.65 ppm in V2-Q1, to 2.8 ppm in V3-Q1, and then increase sharply to 27 ppm in V4-Q1 (Fig. 8A, D). Aluminum concentrations vary more widely than any other element, with an average of 80 ppm in

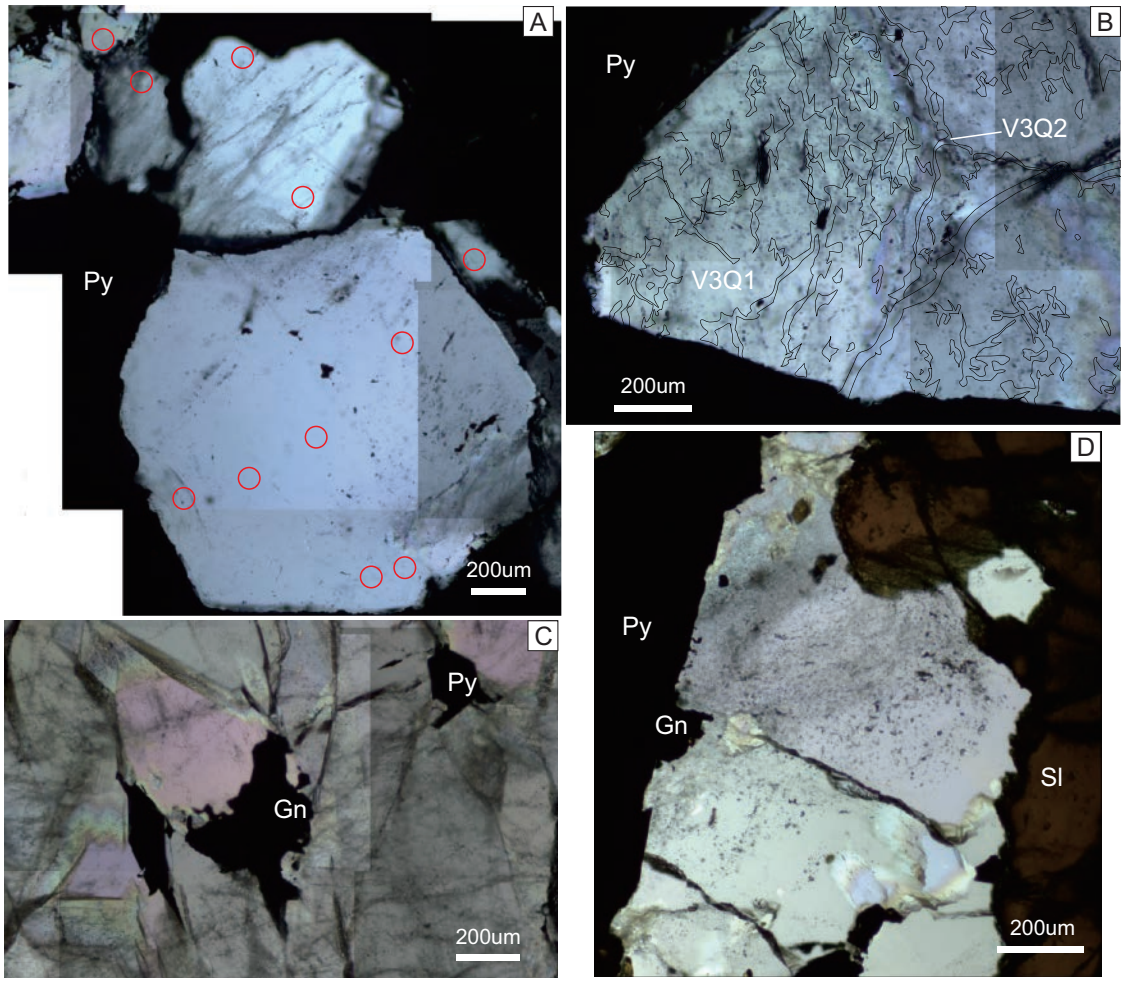

Fig. 6. Transmitted light images of V3, V4, and VS veins. A, B. Transmitted light images of a V3 vein (5101-2). C. Transmitted light image of a V4 vein (DBS13-20). D. Transmitted light image of the strata-bound deposit quartz (DBS12-25). Corresponding CL images are presented in Figure 7. Gn = galena, Py = pyrite.

V1-Q1 and V2-Q1, 118 ppm in V3-Q1, and 667 ppm in V4-Q1 (Fig. 8B, D). Germanium concentrations in V1-Q1, V2-Q1, and V3-Q1 are similar with averages, ranging from 1.4 to 2.2 ppm. Like the other elements, Ge concentrations increase sharply in V4-Q1 to 12 ppm (Fig. 8C, E). The concentration of Ti, Li, Al, and Ge in VS-Q1 fall between values measured in V3-Q1 and V4-Q1 (Fig. 8, Table 2).

No correlations among Ti, Li, Al, and Ge are observable in individual vein generations V1-Q1, V2-Q1, or VS-Q1 (Fig. 8). A weak correlation between Al and Ti is present in each sample in V3-Q1, but there is no correlation among the other elements. Linear correlations among Ti, Li, Al, and Ge are present in V4-Q1 with the following correlation coefficients: Ti-Li (slope = 1.2868, r^2 = 0.5444), Ti-Al

Table 2. Titanium, Li, Al, and Ge Concentrations in Different Generations of Quartz

Sample type	Quartz generation	Ti (ppm)	Li (ppm)	Al (ppm)	Ge (ppm)
V1	V1-Q1	24~89 (30~50)	< 0.1~1.6, avg = 0.38	36~176, avg = ~89	0.76~3.6, avg = 1.4
V2	V2-Q1	10~65 (10~20)	< 0.1~3.5, avg = 0.65	36~150, avg = 72	0.70~3.3, avg = 1.7
V3	V3-Q1	1.5~12 (3~7)	0.47~13, avg = 2.8	36~303, avg = 118	1.0~5.6, avg = 2.2
V4	V4-Q1	0.54~5.3 (0.5~1.5)	0.90~79, avg = 27	45~2005, avg = 667	1.2~29, avg = 12
VS	VS-Q1	0.74~3.3 (1~2)	1.2~10, avg = 3.3	67~239, avg = 131	1.1~3.5, avg = 1.9
V1	V1-Q2	2.9~7.5, avg = 4.8	0.11~0.22, avg = 0.18	98~119, avg = 111	2.4~3.3, avg = 2.9
V2	V2-Q2	4.8~7.3, avg = 5.8	0.11~0.41, avg = 0.23	28~80, avg = 45	1.5~2.5, avg = 2.0
V3	V3-Q2	0.11~1.4, avg = 0.48	< 0.1~0.98, avg = 0.50	20~194, avg = 63	0.26~3.6, avg = 1.6
V4	V4-Q2	-	-	-	-
VS	VS-Q2	0.44~1.7, avg = 0.87	0.22~0.56, avg = 0.34	6.3~130, avg = 42	1.9~4.6, avg = 3.3

Notes: Titanium values in parentheses represent the majority of the data range; - = no data

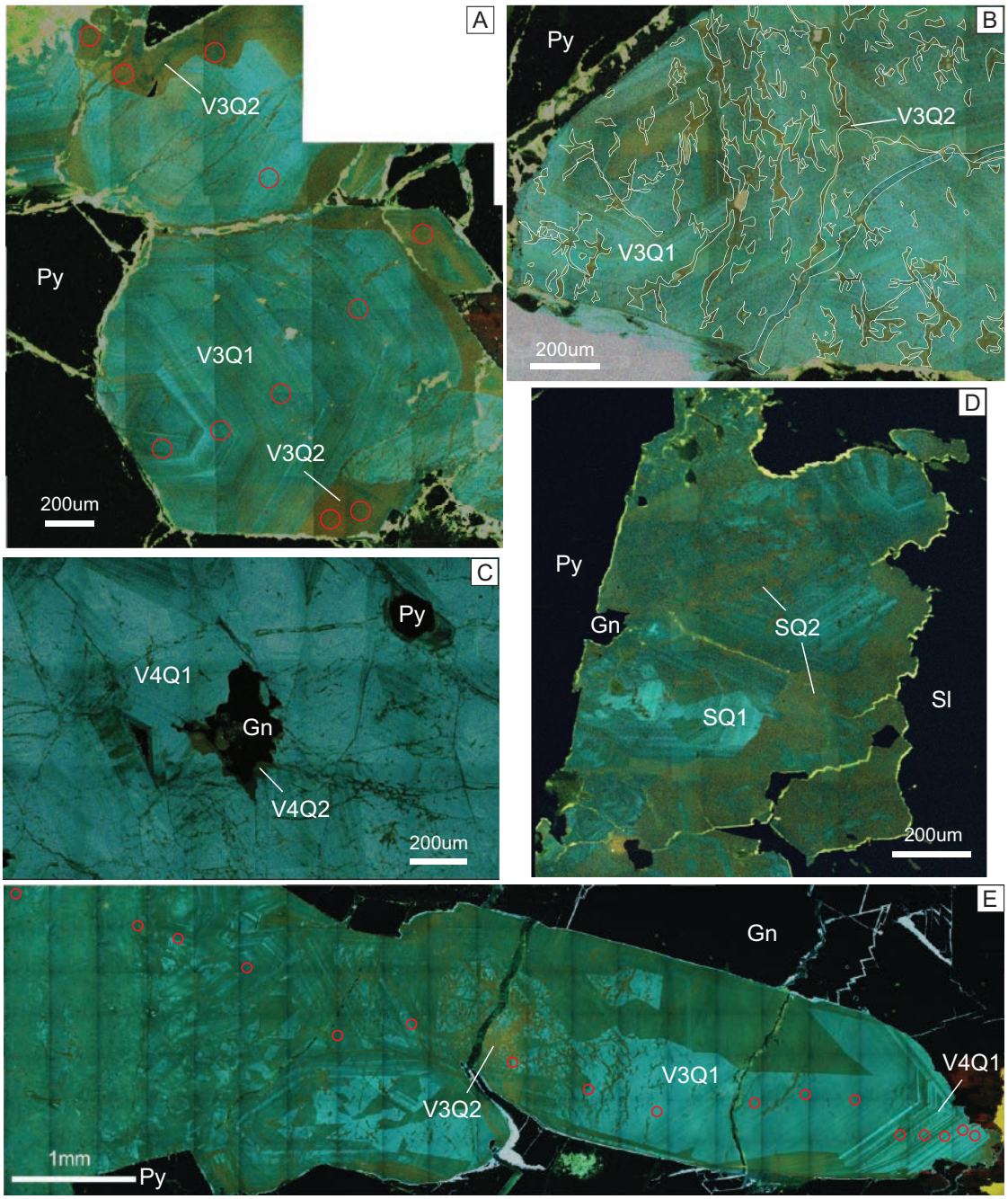

Fig. 7. SEM-CL textures of the quartz-bearing veins in Dabaoshan samples. A, B. SEM-CL textures of a V3 vein (5101-2). Late dark brown to red V3-Q2 quartz has filled fractures and boundaries between V3-Q1 and sulfides. C. SEM-CL textures of a V4 vein (DBS13-20). Sulfides are partly surrounded by late dark brown to red quartz (V4-Q2). D. SEM-CL textures of the strata-bound deposit quartz (DBS12-25). Late dark brown to red quartz veins (VS-Q2) are filled in the fractures and the boundaries between VS-Q1 and the sulfides. E. SEM-CL textures showing the transition from V3 vein to V4 vein (DBS13-16). Red circles mark the laser ablation spots of 80-μm diameter, corresponding trace element data are plotted in Figure 18. Image brightness settings were maximized in every figure for better demonstration of the CL texture. Gn = galena, Py = pyrite. Sl = sphalerite.

(slope = 1.1019, r^2 = 0.5911), Ti-Ge (slope = 0.7230, r^2 = 0.3984), Li-Al (slope = 0.7944, r^2 = 0.9308), Li-Ge (slope = 0.5683, r^2 = 0.7531), and Al-Ge (slope = 0.6803, r^2 = 0.7300). Comparing data from all quartz vein generations, a generally negative correlation exists between Ti and Li (slope = –0.9686, r^2 = 0.5895; Fig. 8A). Generally positive correlations are documented between Li and Al, Li and Ge, and Al and Ge, when considering data from all samples (Fig. 8D-F).

In all vein types, the late dark brown to red quartz (Q2) is typically thin and irregular, thus very limited data were acquired for CL-dark Q2 in V1, V2, V3, and VS veins, and no data were acquired in V4-Q2 (Fig. 9A, B, Table 2). Average Ti concentrations in V1-Q2 and V2-Q2 are 4.8 and 5.8 ppm, respectively,

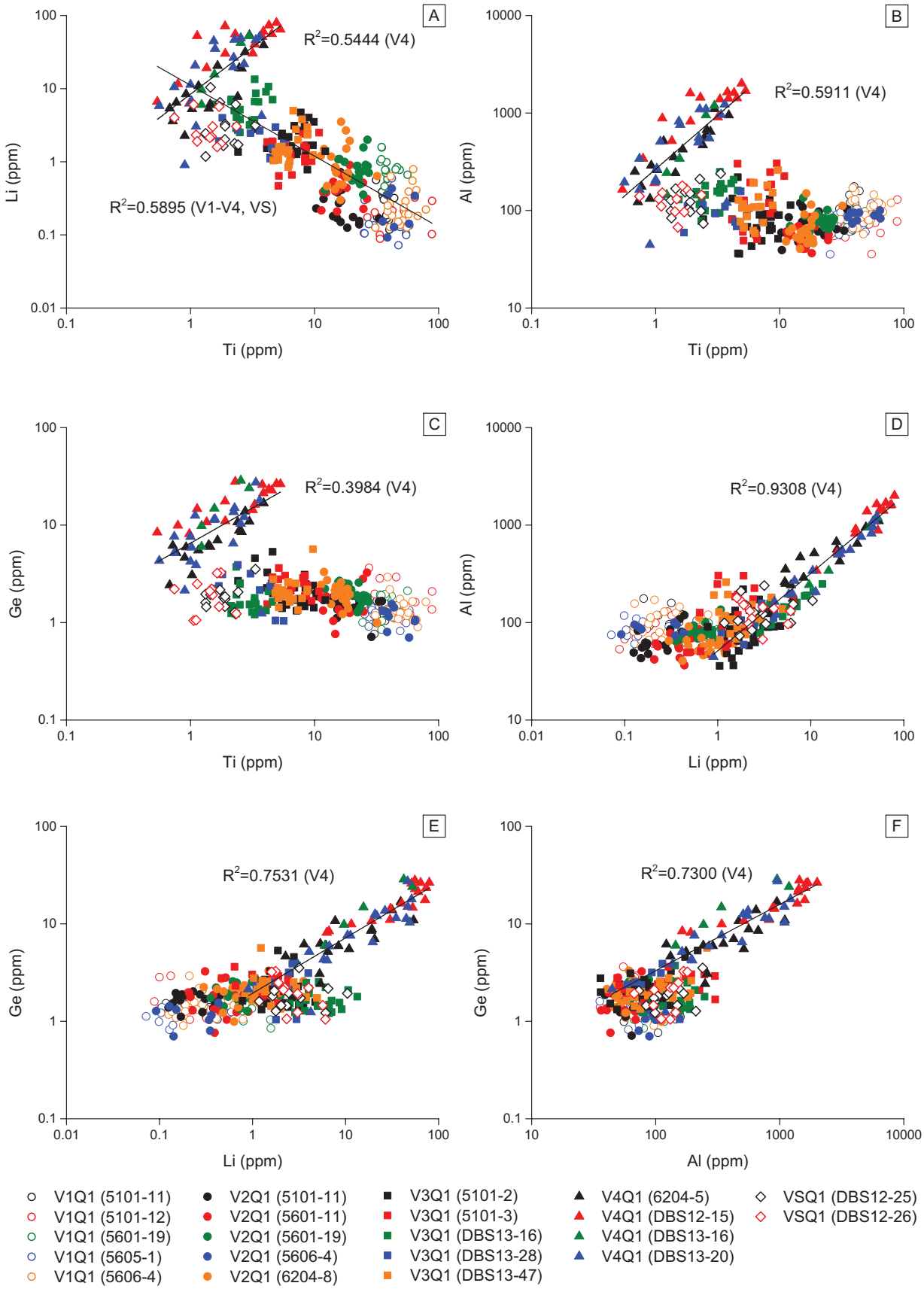

Fig. 8. Concentrations of Ti, Li, Al, and Ge in quartz from the Dabaoshan district.

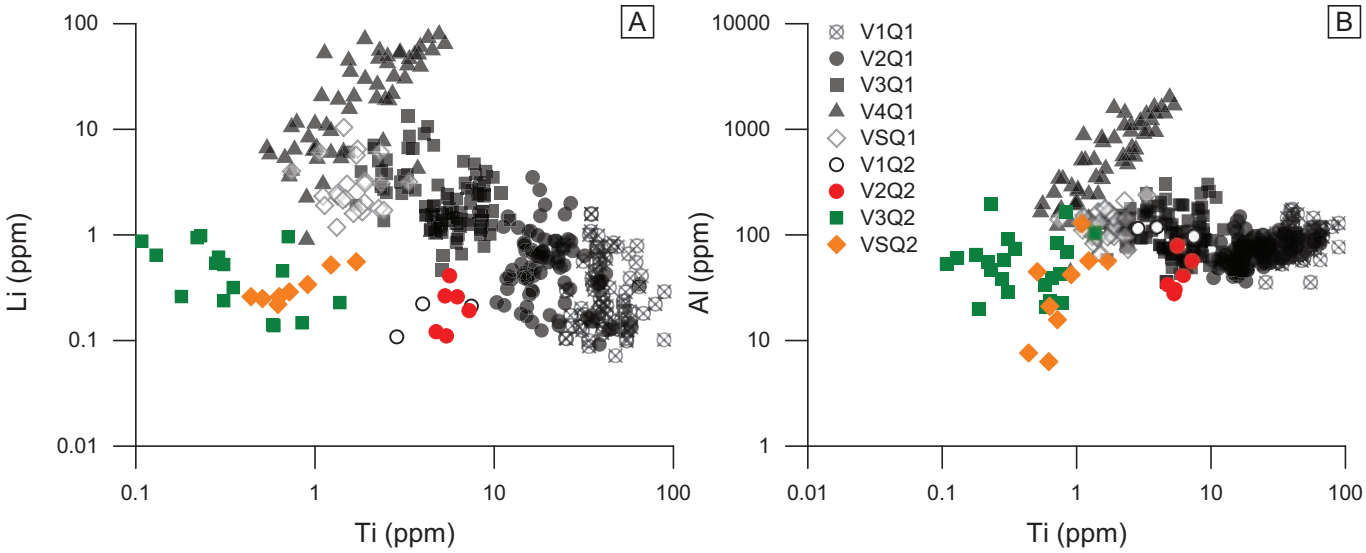

Fig. 9. Concentrations of Ti vs. Li and Ti vs. Al of late dark brown to red quartz (Q2) from V1 to VS veins at Dabaoshan (gray spots in the background are extracted from Fig. 8A and B; crosses are overlapped in circles representing V1 veins for better demonstration).

and decrease to 0.48 ppm in V3-Q2 and 0.87 ppm in VS-Q2. Lithium and Ge concentrations are indistinguishable among vein types and range from <0.1 to 1 ppm, and 1.5 to 5 ppm, respectively, in all the above vein generations. Aluminum concentrations are also indistinguishable in Q2 among all vein types and range from 6.3 up to 194 ppm among all vein generations.

Although in many analyses, we discard Mn, Fe, Cu, As, Sb, and Pb, as we infer the analyses are contaminated by tiny mineral and fluid inclusions, in about 20% of all analyses, some or all of these elements were convincingly unaffected by contamination (see "Methods" above), and we interpret that the concentrations measured to be real and represent structurally bound quartz trace element concentrations. These data are indicated with a * in Appendices 1 to 6 and plotted in Figure 10. Average concentrations of Mn, Fe, Cu, As, Sb, and Pb are summarized in Table 3. The concentrations of Mn, Cu, and As are low and indistinguishable among all vein types, however, Fe concentrations generally decrease whereas Sb and Pb concentrations increase from V1-Q1 to V4-Q1 (Fig. 10B, E, F).

Fluid inclusion petrography

Fluid inclusions from every quartz-bearing vein generation and the late calcite veins were observed and analyzed to constrain fluid compositions, pressures, and temperatures. Fluid inclusions were categorized based on the phases observable at room temperature, where the letter B denotes bubble and the number after the letter B denotes the average volume percent of bubble size. For example, B35 indicates an inclusion containing 35 vol % vapor and 65 vol % liquid. Carbon dioxide-rich inclusions, where liquid and gaseous CO_2 are both observable at room temperature (double bubble fluid inclusions) are referred to as DB# where the letters DB stand for "double bubble" and the number refers to the average volume percent of liquid CO_2 + vapor CO_2.

Criteria for the identification of primary fluid inclusions includes inclusions trapped along the growth zones or inclusions scattered randomly throughout a quartz crystal (Roedder, 1984; Goldstein, 2003). Most fluid inclusions at Dabaoshan are scattered as clusters haphazardly throughout quartz grains, although some B20 inclusions are aligned on trails. Fluid inclusions measured in this study are from clusters of fluid inclusions with similar vapor/liquid ratios distributed throughout the quartz grains, and are not secondary inclusions located in linear arrays along healed fractures. If a group of fluid inclusions with similar phase proportions at room temperature yields similar melting and homogenization temperatures, we infer that they are a primary assemblage, with respect to their quartz host, as distinguished via CL.

Whereas some inclusions appear to be hosted within CL-dark Q2 in V1, V2, and V3 veins, there is not a consistent correlation between this patchy CL-dark quartz and fluid inclusion distributions. For example, primary and secondary fluid inclusions are present both inside and outside of the CL-dark Q2 in V3 veins (compare Fig. 6B and Fig. 7B). Recent work by Lambrecht and

Table 3. Average Concentrations of Mn, Fe, Cu, As, Sb, and Pb in Different Generations of Quartz

Sample type	Quartz generation	Mn (ppm)	Fe (ppm)	Cu (ppm)	As (ppm)	Sb (ppm)	Pb (ppm)
V1	V1-Q1	0.16	2.3	0.25	0.40	0.05	0.10
V2	V2-Q1	0.18	1.4	0.35	0.39	0.05	0.10
V3	V3-Q1	0.19	0.64	0.34	0.55	0.12	0.12
V4	V4-Q1	0.22	0.37	0.36	0.97	0.58	0.54
VS	VS-Q1	0.18	0.41	-	-	0.12	0.54

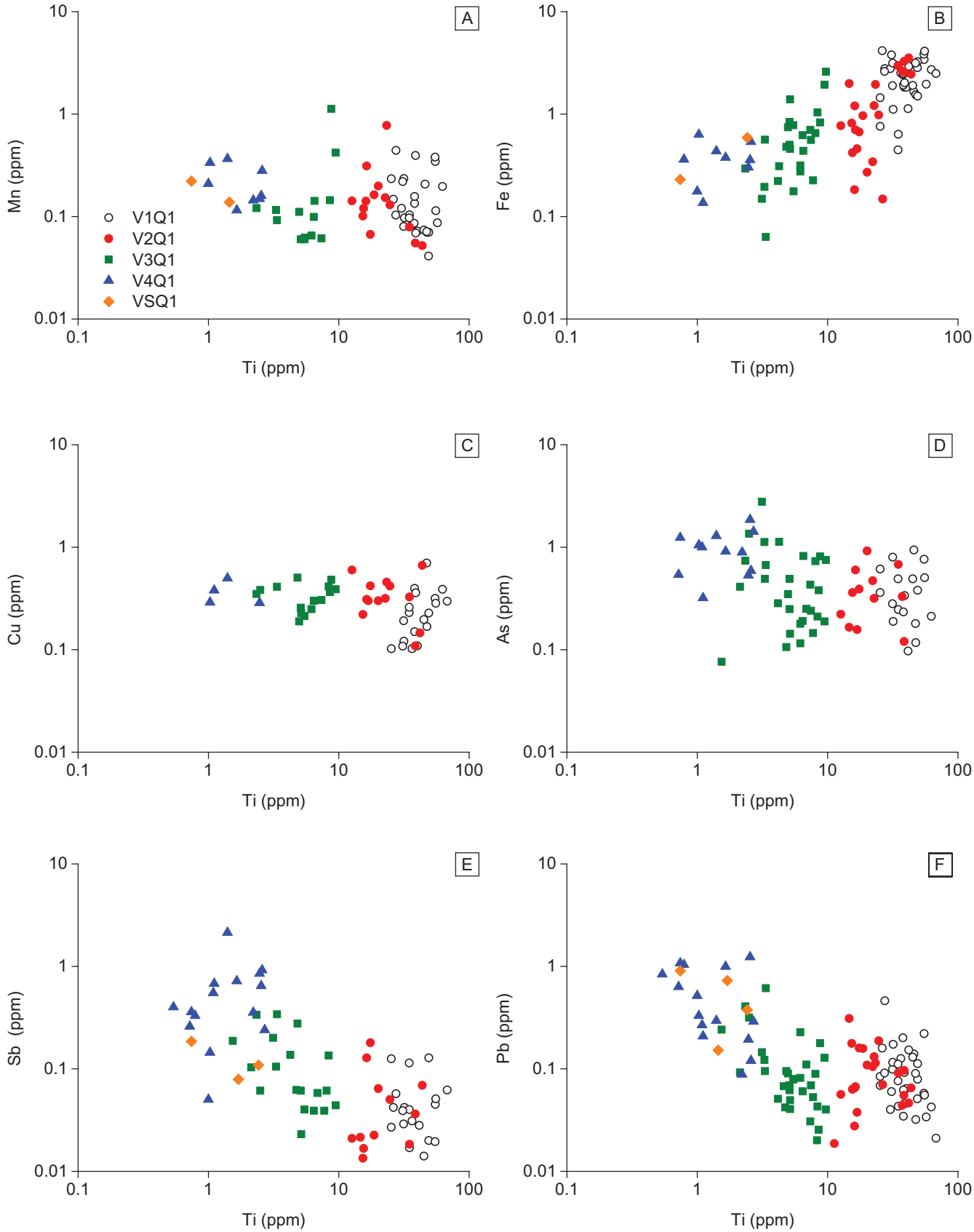

Fig. 10. Selected fluid/mineral inclusion-free data of Mn, Fe, Cu, As, Sb, and Pb from V1 to VS veins at Dabaoshan. Changes of trace element concentrations over the various stages of veins are defined by Fe, Sb, and Pb.

Diamond (2014) shows the genetic relationship between the CL-dark patches and the spontaneous morphological ripening of preexisting fluid inclusions. Driven by the potential to reduce surface free energy of fluid inclusions, solvent water in the fluid inclusions perpetually dissolves and reprecipitates the inclusion walls, thereby sequestering trace elements (e.g., Li, Al, Na, and Ti). The purified host quartz becomes nonluminescent in the process. Total volume of fluid and its bulk composition (and hence fluid density) were confirmed to be conserved during the fluid inclusion ripening (Lambrecht and Diamond, 2014). They concluded, and we concur, that splatter and cobweb texture is not caused by influx of an external fluid, but rather by volume-conserved modification of existing fluid inclusions. Inclusions hosted in CL-dark splatter and cobweb quartz (i.e., Q2 in V1, V2, and V3 from Dabaoshan) are therefore interepred to be primary with repsect to the CL-bright (Q1) quartz that hosts the inclusions, even in regions where the inclusions coincide with CL-dark Q2 patches.

Table 4 summarizes the classification and distributions of fluid inclusions in quartz from all vein types (Fig. 11). Primary fluid inclusions in V1 and V2 veins consist of ~70 to 90% B35 inclusions and ~10 to 30% DB40 inclusions, respectively (Table 4). No difference in fluid inclusion populations was recognized between V1 and V2 veins (Fig. 11A-D). Approximately 5 to 20% of the B35 inclusions and ~5% of the DB40 inclusions in V1 and V2 veins contain an opaque daughter mineral. Primary fluid inclusions in V3 veins tend to have larger vapor bubbles and these veins contain around 85% B45 inclusions and around 15% DB50 inclusions (Fig. 11E-H). Nearly 10% of B45 inclusions and ~5% DB50 inclusions in V3 veins contain an opaque daughter mineral. Secondary B20 fluid inclusions are more common in V3 than in earlier vein generations (Fig. 11G, I). V4 veins have fluid inclusion populations consisting of more than 90% B20 inclusions and less than 10% DB25 inclusions (Fig. 11J-L). Less than 15% of the B20 inclusions in V4 veins contain one opaque daughter mineral. Around 5 to 10% of the opaque daughter minerals in all vein types have triangular shapes, indicating that they are likely to be chalcopyrite. No hematite daughter minerals were observed in any fluid inclusion. Fluid inclusions from the strata-bound deposit are distinct from those in the porphyry-related quartz-bearing veins. VS veins contain approximately 75% B85 inclusions, 15% DB70 inclusions, and ~10% B20 inclusions (Fig. 11M-Q). The volume fraction of liquid CO_2 + vapor CO_2 in CO_2-rich inclusions in strata-bound quartz typically shows a larger variation than the vapor phase proportion in two-phase inclusions. Fluid inclusions in the strata-bound quartz rarely contain opaque daughter minerals. Calcite veins only host two-phase fluid inclusions with an average bubble size of ~5 vol % (Fig. 11R-T). No CO_2-rich three-phase fluid inclusions were observed in calcite veins.

Unlike nearly all other porphyry-type ore deposits, very few halite-bearing inclusions were identified in any vein from the Dabaoshan porphyry deposit. Out of thousands of fluid inclusions observed in over 50 petrographic thick sections, only two assemblages of halite-bearing fluid inclusions were identified; one in a V3 vein (DBS13-28) and one in a VS vein (DBS12-25; Fig. 11Q). In both cases, the inclusions were too

Table 4. Classification and Abundances of Fluid Inclusions in Quartz-Bearing Veins and Calcite Veins

Location	Sample no.	Sample type	Drill hole coordinates (UTMs) E	N	Elevation (m)	B no. B5	B20	B35	B45	B85	DB no. DB25	DB40	DB50	DB70
DBS Granodiorite porphyry	5101-11	V1-Q1	469957	2718435	495			90				10		
DBS Granodiorite porphyry	5101-12	V1-Q1	469957	2718435	509			91				9		
DBS Dacite porphyry	5601-19	V1-Q1	470460	2718007	216			92				8		
DBS Dacite porphyry	5605-1	V1-Q1	470460	2718301	129			94				6		
DBS Granodiorite porphyry	5606-4	V1-Q1	470460	2718440	109			92				8		
DBS Granodiorite porphyry	5606-15	V1-Q1	470460	2718440	405			88				12		
DBS Granodiorite porphyry	5101-11	V2-Q1	469957	2718435	495			85				15		
DBS Granodiorite porphyry	5101-12	V2-Q1	469957	2718435	509			75				25		
DBS Granodiorite porphyry	5601-11	V2-Q1	470460	2718007	478			80				20		
DBS Dacite porphyry	5601-19	V2-Q1	470460	2718007	216			69				31		
DBS Granodiorite porphyry	5606-4	V2-Q1	470460	2718440	109			84				16		
DBS Granodiorite porphyry	5606-15	V2-Q1	470460	2718440	405			88				12		
JQL Dacite porphyry	6204-8	V2-Q1	470760	2718314	–85			83				17		
DBS Granodiorite porphyry	5321-4	V3-Q1	470430	2717610	491				87				13	
DBS Granodiorite porphyry	5101-2	V3-Q1	469957	2718435	351				86				14	
DBS Granodiorite porphyry	5101-3	V3-Q1	469957	2718435	507				85				15	
Devonian limestone	DBS13-16	V3-Q1	471106	2717450	756				78				22	
Devonian limestone	DBS13-28	V3-Q1	471202	2718300	688				82				18	
DBS Granodiorite porphyry	DBS13-47	V3-Q1	470134	2718215	646				93				7	
JQL Dacite porphyry	6204-5	V4-Q1	470760	2718314	703		99				1			
Devonian limestone	DBS12-15	V4-Q1	470958	2717557	780		97				3			
Devonian limestone	DBS13-16	V4-Q1	471106	2717450	756		95				5			
DBS Dacite porphyry	DBS13-20	V4-Q1	471038	2717465	753		90				10			
Devonian limestone	DBS12-25	VS-Q1	471432	2716544	784		10			75				15
Devonian limestone	DBS12-26	VS-Q1	471282	2717260	755		8			76				16
JQL Dacite porphyry	6204-4	VC	470760	2718314	709	100								
Devonian limestone	DBS12-8	VC	470900	2717639	780	100								

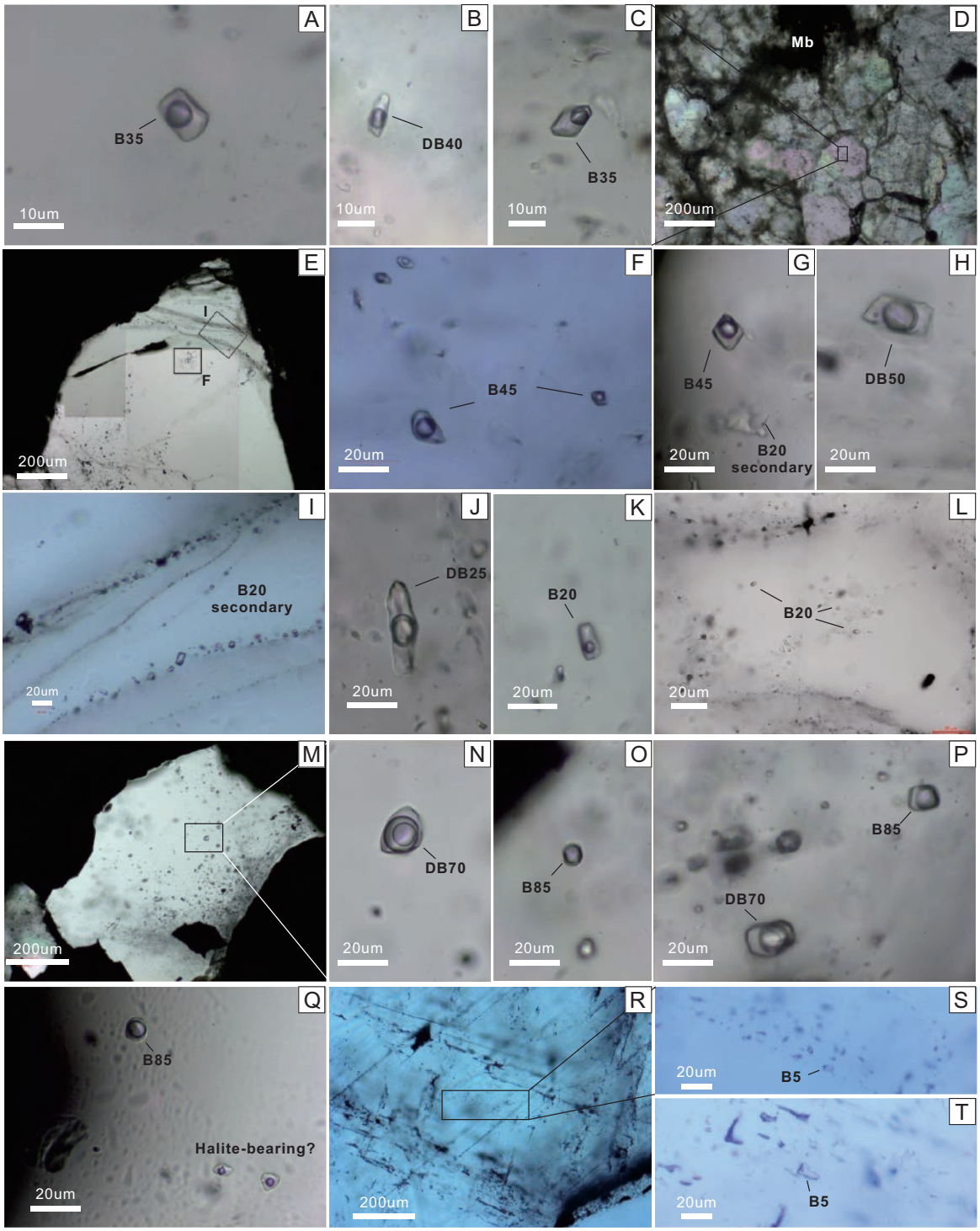

Fig. 11. Transmitted light images of fluid inclusions in Dabaoshan. A. A B35 fluid inclusion containing ~35 vol % bubble in a V1 vein (5101-11). B. A DB40 fluid inclusion in a V1 vein with ~40 vol % of liquid CO_2 + vapor CO_2 (5605-1). C. A B35 fluid inclusion in a V2 vein (5601-11). D) V2 vein quartz (5601-11). E. V3 vein quartz (5101-2). F) B45 fluid inclusions in a V3 vein, containing 35 to 50 vol % bubble (5101-2). G. A B45 fluid inclusion in a V3 vein (DBS13-47). H. A DB50 fluid inclusion in a V3 vein with ~50 vol % of liquid CO_2 + vapor CO_2 (DBS13-47). I. Secondary B20 fluid inclusions filling in the fracture of a V3 vein (5101-2). J. A DB25 fluid inclusion in a V4 vein with ~25 vol % liquid CO_2 + vapor CO_2 (DBS12-15). K. A B20 fluid inclusion in a V4 vein (DBS13-16). L. Randomly distributed B20 fluid inclusions in a V4 vein (DBS13-20). M. VS quartz with abundant fluid inclusions (DBS12-25). N. A DB70 fluid inclusion in a VS vein with ~70 vol % liquid CO_2 + vapor CO_2 (DBS12-25). O. A B85 fluid inclusion in a VS vein containing ~85 vol % bubble (DBS12-25). P. Coexisting B85 and DB70 fluid inclusions in a VS vein (DBS12-26). Q. A B85 fluid inclusion and halite-bearing fluid inclusions (?) in a VS vein (DBS12-25). R. B5 fluid inclusions distributed along the growth zones in a calcite vein (6204-4). S. B5 fluid inclusions in a calcite vein (6204-4). T. A B5 fluid inclusion in a calcite vein (DBS12-8). Mb = molybdenite.

small (<5 μm) to measure by microthermometry. Vapor-dominated fluid inclusions, commonly coexisting with halite-bearing inclusions in most porphyry systems, are also generally absent in Dabaoshan, with the exception of B85 inclusions in VS veins, which condense a liquid CO_2 phase upon cooling below 5°C (See next section).

Fluid inclusion microthermometry

Nearly all of the B35 and B45 inclusions and ~70% of the B20 inclusions in quartz from V1 to V4 and VS veins formed clathrate upon cooling. No CO_2 was observed at room temperature in these fluid inclusions, and solid CO_2 never formed, even upon cooling to temperatures below –100°C. Therefore, both clathrate and ice melting temperatures were measured to accurately determine the salinity, density, and CO_2 concentrations of the fluids (Figs. 12, 13). Clathrate never formed in any fluid inclusion in the late calcite veins.

Ice and clathrate melting temperatures of two-phase fluid inclusions (B35, B45, and B20) in all quartz-bearing veins (V1-V4) range from –9.5° to –2.2°C and +5.2° to +9.3°C, respectively (Table 5, Fig. 12). Calculated salinities were consistently low from early to late, ranging from 1.0 to 7.3 wt % NaCl equiv. CO_2 concentrations vary from 3.7 to 10 mol %. All two-phase fluid inclusions homogenized to liquid. Homogenization temperatures in B35 fluid inclusions from V1 and V2 veins are similar and average ~290°C. In V3 veins, where bubble sizes are slightly larger (B45), average homogenization temperatures increase to ~306°C. B20 inclusions in V4 homogenize at much lower temperatures of ~220°C. Calculated fluid densities range from 0.64 to 0.74 g/cm^3 in V1, 0.66 to 0.74 g/cm^3 in V2, 0.56 to 0.69 g/cm^3 in V3, and 0.75 to 0.89 g/cm^3 in V4.

Solid CO_2 melting temperatures of CO_2-rich three-phase fluid inclusions in V1 to V4 range from –56.3° to –56.9°C, indicating that CO_2 is the dominant gas. Clathrate melting temperatures range from 4.5° to 8.5°C (Fig. 12), and calculated salinities range from 2.6 to 9.6 wt % NaCl equiv. CO_2 concentrations vary from 6.6 to 17 mol %, nearly twice of that in two-phase fluid inclusions mentioned above. Homogenization temperatures and calculated salinities of CO_2-rich three-phase fluid inclusions in each vein generation are correspondingly higher than two-phase fluid inclusions (Table 5).

Fluid inclusions in quartz from the VS veins are distinct from fluid inclusions in V1 to V4 veins. They contain larger vapor bubbles in two-phase fluid inclusions and larger liquid CO_2 + vapor CO_2 volumes in the three-phase fluid inclusions (Fig. 11M-Q) compared to V1 to V4 veins. Most of the B85 inclusions condense a liquid CO_2 phase upon cooling below 5°C, indicating that they are also CO_2 rich. Homogenization of liquid CO_2 + vapor CO_2 in B85 inclusions occurred between 8.4° to 22.3°C (Fig. 13). The melting temperatures of solid CO_2 in B85 and DB70 inclusions can be as low as –60.2°C, and clathrate melting temperatures range from 9.2° to 14.5°C for B85 inclusions and 9.1° to 10.2°C for DB70 inclusions, respectively (Table 5, Fig. 13). Such low solid CO_2 melting temperatures and high clathrate dissolution temperatures indicate the presence of other gaseous components in addition to CO_2, most likely CH_4 or N_2. Therefore, the salinity, CO_2 content, and fluid density cannot be accurately calculated without knowing the concentrations of these gaseous components. Data listed in Table 5 were acquired by

Table 5. Microthermometric Properties of Fluid Inclusions

Sample type	Inclusion type	Ice melting temperature (°C)	Solid CO_2 melting temperature (°C)	Clathrate melting temperature (°C)	Bubble volume range (%)	Homogenization temperature range (°C)	Salinity (wt % NaCl equiv)	Mol % of CO_2	Density (g/cm^3)
V1–Q1	B35 (n = 44)	–3.1 to –5.8		5.2–9.1	30–40	248–331, avg = 287	2.2–4.9, avg = 3.5	4.1–10, avg = 5.2	0.64–0.74
	DB40 (n = 11)		–56.5 to –56.9	4.6–7.6	35–45	278–315, avg = 298	4.2–9.6, avg = 6.2	8.3–14, avg = 10	0.70–0.77
V2–Q1	B35 (n = 29)	–2.2 to –5.8		5.2–8.7	30–45	256–315, avg = 291	1.0–5.5, avg = 3.3	3.9–6.2, avg = 4.9	0.66–0.74
	DB40 (n = 11)		–56.3 to –56.8	6.3–7.8	35–50	298–328, avg = 317	3.9–6.6, avg = 5.2	9.5–12, avg = 10	0.68–0.76
V3–Q1	B45 (n = 32)	–3.3 to –7.3		6.1–9.3	35–50	253–358, avg = 306	2.6–5.4, avg = 4.1	4.4–6.8, avg = 5.7	0.56–0.69
	DB50 (n = 85)		–56.4 to –57.6	4.5–7.8	35–55	274–357, avg = 306	5.7–6.6, avg = 6.3	12–17, avg = 14	0.62–0.74
V4–Q1	B20 (n = 83)	–3.5 to –9.5		5.8–8.5	15–25	183–278, avg = 221	4.2–7.3, avg = 5.7	3.7–4.9, avg = 4.3	0.75–0.89
	DB25 (n = 8)		–56.3 to –56.9	5.5–8.5	20–30	268–303, avg = 273	2.6–8.0, avg = 5.4	6.6–7.6, avg = 7.2	0.77–0.83
VS–Q1	B85 (n = 51)	–3.1 to –6.3	–57.4 to –60.2	9.2–14.5	65–90	283–333, avg = 306	0.04–1.2, avg = 0.58	50–66, avg = 55	0.78–0.87
	DB70 (n = 16)		–57.7 to –59.3	9.1–10.2	75–85	308–323, avg = 305	0.23–1.4, avg = 0.65	48–58, avg = 53	0.73–0.82
VC	B5 (n = 44)	–2.8 to –0.2			5 –10	99–168, avg = 123	0.35–4.7, avg = 2.3		0.90–0.97

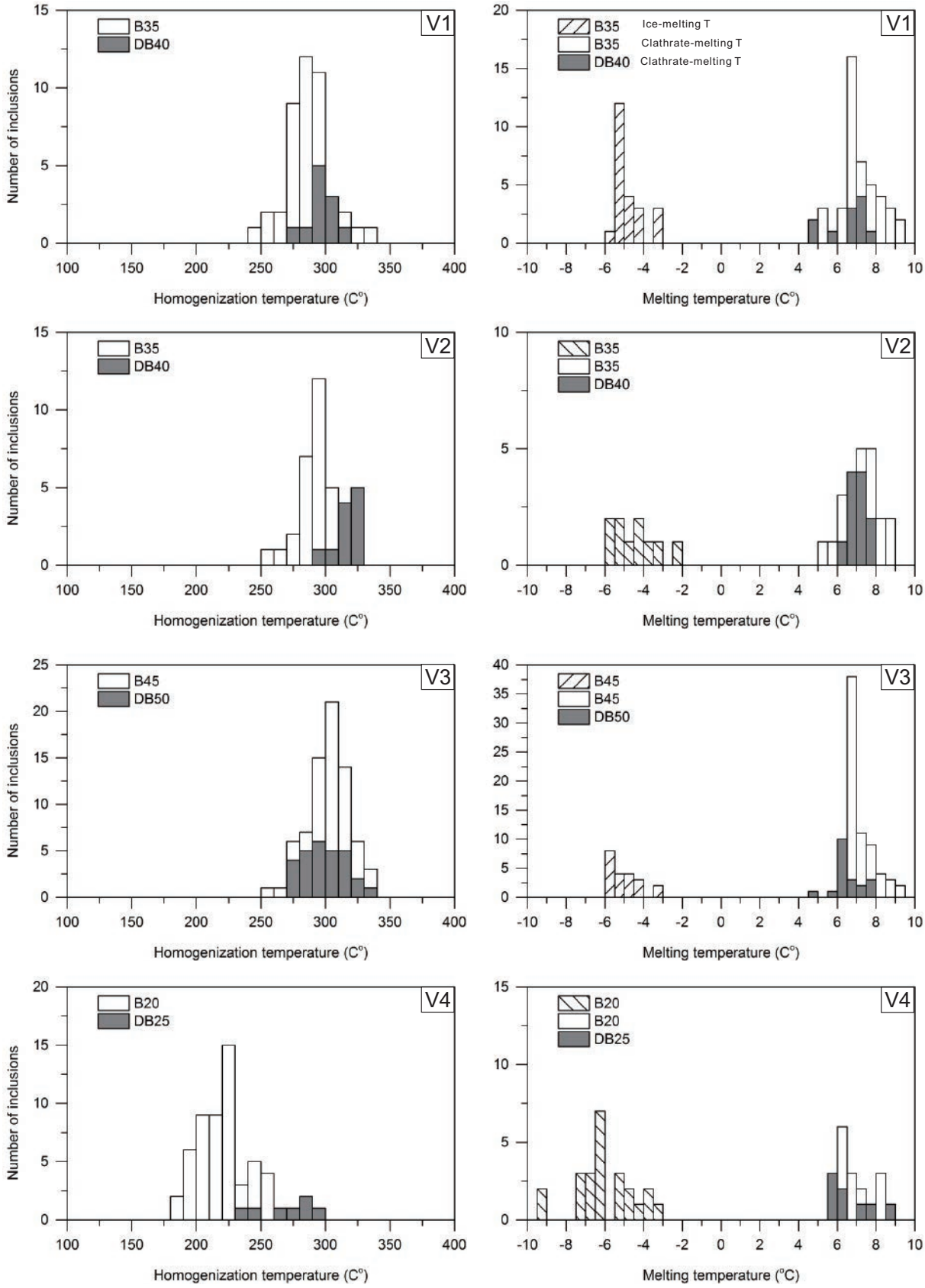

Fig. 12. Histograms showing homogenization and melting temperatures of ice and clathrates in fluid inclusions in V1 to V4 veins in Dabaoshan. Clathrate formed in the majority of the vapor-liquid inclusions in quartz-bearing veins upon cooling.

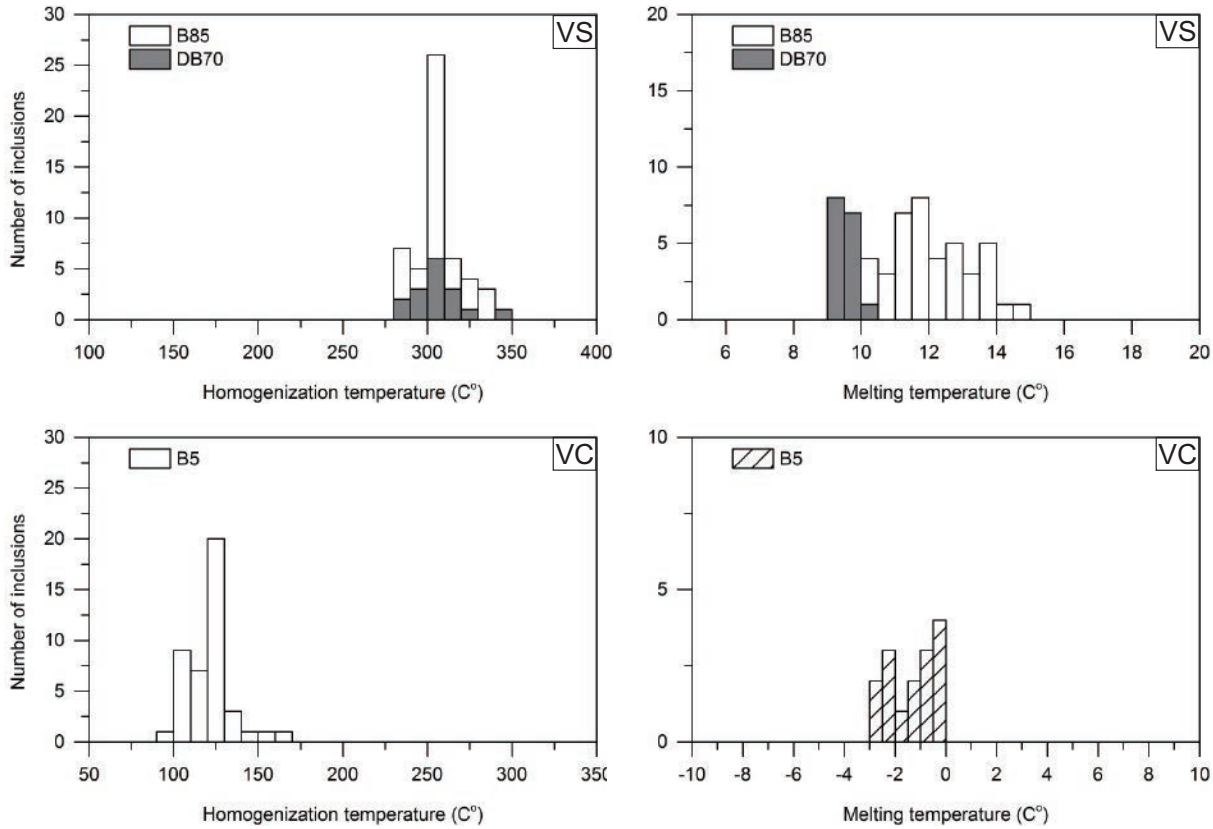

Fig. 13. Histograms showing homogenization and melting temperatures of ice and clathrates in fluid inclusions in VS and VC veins from Dabaoshan.

assuming no CH_4 or N_2 in inclusions with clathrate melting temperatures lower than 9.8°C. Salinities calculated for B85 and DB70 inclusions range from 0.04 to 1.2 wt % NaCl equiv and 0.23 to 1.4 wt % NaCl equiv, respectively. CO_2 concentrations vary between 50 and 66 mol % for B85 inclusions and 48 to 58 mol % for DB70 inclusions, which are nearly 5 to 10 times the CO_2 concentrations of fluid inclusions in V1-V4 veins. Calculated fluid densities range from 0.78 to 0.87 g/cm^3 for B85 inclusions and 0.73 to 0.82 g/cm^3 for DB70 inclusions. Homogenization of B85 and DB70 occurred either by fading of the meniscus between the liquid CO_2 and aqueous fluid or by homogenization to vapor. Homogenization temperatures of B85 and DB70 inclusions are identical at around 305°C, with most between 290° to 310°C (Fig. 13).

B5 fluid inclusions are dominant in the calcite veins (Fig. 11R-T). Ice melting temperatures range from –2.8 to –0.2°C (Fig. 13), and the corresponding salinities vary from 0.35 to 4.7 wt % NaCl equiv. No clathrates were observed in these inclusions. Homogenization temperatures are much lower than the above fluid inclusions, ranging from 99° to 168°C. Calculated fluid densities vary from 0.90 to 0.97 g/cm^3.

Sulfur, hydrogen, and oxygen isotope compositions

Although no new isotopic results were obtained in this study, we summarized H, O, and S isotope data from the literature here, in order to reinterpret them in conjunction with our new fluid inclusion data. Pyrite disseminated in the upper Devonian Tianziling limestone has $\delta^{34}S$ values ranging from +8.7 to +17.9‰, while pyrite disseminated in the middle Devonian Donggangling limestone has $\delta^{34}S$ values ranging from –22.5 to –5.2‰ (Xu et al., 2008). $\delta^{34}S$ values of sulfides from porphyry-hosted quartz-bearing veins ranges from –4 to +4‰, with an average of ~0.1‰, while $\delta^{34}S$ values of sulfides from the strata-bound deposit varies from –4 to +5‰, with an average of ~+0.4‰ (Song et al., 2007; Xu et al., 2008).

Hydrogen isotope compositions of the fluid inclusions preserved in V2 veins and VS veins are around –56.1 and –50.7‰, respectively (Cai and Liu, 1993b). Oxygen isotope compositions for quartz and muscovite from previous studies have been reclassified according to our sample classification (Table 6). In the original studies, fluid inclusion homogenization temperatures, with no isochoric corrections, were used to calculate isotopic fractionation between water and minerals by oxygen isotope thermometers (O'Neil and Taylor, 1969; Clayton et al., 1972), leading to low calculated $\delta^{18}O$ values of water (Ge and Han, 1986; Cai and Liu, 1993b). Here, new $\delta^{18}O$ values of water are recalculated based on temperatures of vein formation inferred from using isochoric corrections to the actual fluid inclusion trapping conditions (Table 6, Fig. 14).

Discussion

CL textures, trace elements, and physiochemical conditions of hydrothermal mineralization

Few comprehensive studies integrating CL textures and trace elements in successive generations of vein quartz in porphyry

Table 6. Oxygen Isotope Composition in Quartz and Muscovite

Sample no.	Type	This study	Mineral	$\delta^{18}OQz/‰$	Temperature/°C[1]	$\delta^{18}OH_2O/‰$
D925-1	Molybdenite quartz vein hosted in granodiorite	V2	Quartz	13.2	530	11.3
CZK210-3	Molybdenite quartz vein hosted in granodiorite	V2	Quartz	11.6	530	9.7
DZK1055-1	Molybdenite quartz vein hosted in granodiorite	V2	Muscovite[2]	11.8	400	10.4
D760-4	Pyrite quartz vein hosted in granodiorite	V3	Quartz	13.5	400	9.4
D925-2	Pyrite quartz vein hosted in granodiorite	V3	Quartz	13.4	400	9.3
ZK2026-77	Massive pyrite ore (P. 27)[3]	VS	Quartz	15.0	350	9.7
ZK2026-75	Massive pyrite ore (P. 27)	VS	Quartz	15.9	350	10.6
ZK2026-792	Massive pyrite ore (P. 27)	VS	Quartz	15.8	350	10.5
ZK2038-133	Massive pyrite ore (P. 11)	VS	Quartz	13.0	325	6.9
ZK2038-1632	Massive pyrite ore (P. 11)	VS	Quartz	12.4	325	6.3
ZK2029-243	Massive Pb-Zn ore (P. 0)	VS	Quartz	12.9	300	6.0
ZK2029-2405	Massive Pb-Zn ore (P. 0)	VS	Quartz	14.6	300	7.7
ZK2029-242	Massive Pb-Zn ore	VS	Quartz	15.4	300	8.5
ZK2029-241	Massive Pb-Zn ore (P. 0)	VS	Quartz	14.6	300	7.7
ZK2004-365	Massive Pb-Zn ore (P. 10)	VS	Quartz	13.9	275	6.1
ZK2008-108	Massive pyrite ore (P. 16)	VS	Quartz	14.6	275	6.8

Notes: $\delta^{18}OQz$ data are collected from Liu et al. (1985), Ge and Han (1986), and Cai and Liu (1993b); equations used for calculation of $\delta^{18}O$ in water are from Clayton et al. (1972) and O'Neil and Taylor (1969)

[1]Temperature used for calculating $\delta^{18}O$ in water is based on this study; decreasing temperature estimates were made for samples from the strata-bound deposit according to their distance from the Dabaoshan granodiorite (Fig. 1)

[2]Muscovite in quartz-molybdenite veins indicate overprinting from later sercitic alteration, therefore, temperature of 400°C is used for calculation

[3]P. = prospecting line; positions of prospecting lines are illustrated in Figure 1

copper deposits exist (Grasberg, Indonesia: Penniston-Dorland, 2001; Butte, Montana: Rusk and Reed, 2002; Bingham Canyon, Utah: Landtwing and Pettke, 2005; Oyu Tolgoi, Mongolia: Müller et al., 2010; Altar, Argentina: Maydagán et al., 2015). Several consistent observations have been made among the studied deposits. For example, the earliest generations of quartz in all of the above porphyry-type deposits are granular mosaics of CL-bright quartz. In most cases the earliest quartz lacks internal growth zonations and instead displays homogeneous granular mosaic textures. Such quartz commonly has relatively high Ti concentrations which range from several tens of ppm to ~150 ppm. Where subsequent generations of quartz are present in a single vein, the later quartz is almost always CL darker than the earlier quartz, and the darker later quartz always contains less Ti than earlier CL brighter quartz generations. At the Dabaoshan porphyry Mo deposit, quartz CL intensity decreases sequentially with time from V1 to V4 veins (Fig. 5, 7). Granular mosaics of CL-bright quartz are present only in V1 and V2 veins, whereas V3, V4, and VS veins are dominated by quartz that has lower CL intensity and with euhedral growth zone textures. Where V3 and V4 veins reopen earlier veins, quartz with lower CL intensity consistently cuts CL-bright quartz. Among all vein generations, CL intensity correlates strongly with Ti concentration, and does not correlate consistently with any other element. V3 and V4 veins from Dabaoshan are similar to D veins from other porphyry deposits in that later CL-dark euhedral quartz from V3 and V4 veins contain up to an order of magnitude more Al than earlier CL brighter V1 and V2 veins. The consistency of these observations among multiple porphyry-type deposits from around the world demonstrates that the similar physical and chemical evolution of fluids in porphyry systems ultimately control quartz chemistry and resultant CL textures.

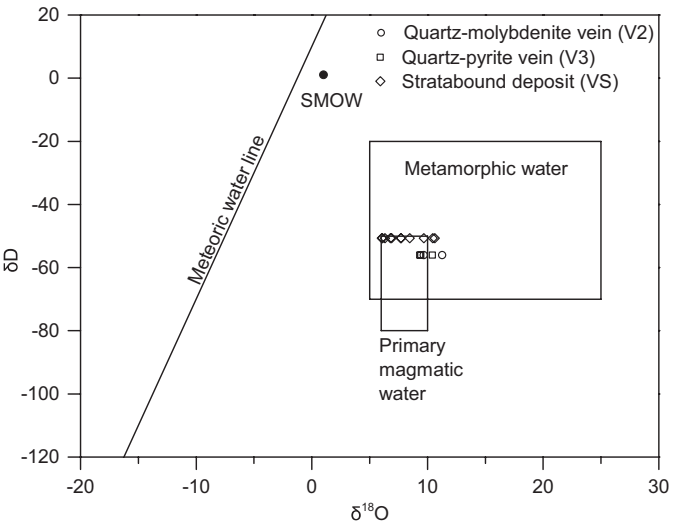

Fig. 14. $\delta^{18}O$-δD diagram of water in hydrothermal fluids from Dabaoshan.

The CL-bright quartz with homogeneous CL textures in V1 and V2 veins is interpreted to reflect high temperatures and pressures early in the life of the Dabaoshan system, as has been inferred in similar deposits (Penniston-Dorland, 2001; Rusk and Reed, 2002; Landtwing et al., 2005; Rusk, 2006; Müller et al., 2010; Maydagán et al., 2015). High Ti concentrations in quartz are consistent with higher temperatures (Huang and Audétat, 2012), and homogeneous CL textures may result from relatively rapid diffusion of Ti at high temperatures, or from an initial lack of texture due to rapid nucleation and precipitation. These textures form at near magmatic pressures and temperatures (see below) under lithostatic load, where quartz solubility is high, open space is restricted, and the host rock is ductile. Later CL-dark euhedral quartz grains in V3, V4, and VS veins, on the other hand, have lower Ti concentrations, which suggest lower temperatures (Huang and Audétat, 2012). They also contain higher Al, which may result from more acidic fluids (cf. Rusk et al., 2008b), consistent with

lower temperature fluids and muscovite and argillic alteration that surrounds V3 and V4 veins. Internal growth zones in V3, V4, and VS quartz crystals suggest growth into open space, and sharp CL intensity boundaries among oscillating growth zones indicate that diffusion of trace elements or recrystallization after initial quartz precipitation was minimal. All these lines of evidence suggest that such crystals precipitated at lower temperatures, likely under more acidic conditions, where the rock was more likely to experience brittle fracturing, leading more frequently to open space. The CL textures and concentrations of Ti, Li, Al, and Ge in successive quartz generations from Dabaoshan are similar to concentrations of these elements in successive vein generations from the Altar porphyry Cu deposit, Argentina (Maydagán et al., 2015).

Pressures and temperatures of vein formation

We calculated pressures and temperatures of vein formation based on the intersections of fluid inclusion isochores with Ti-in-quartz isopleths (Huang and Audétat, 2012). The presence of rutile in V1, V2, and V3 veins indicates that the system was rutile saturated, so a TiO_2 activity of one was assumed for the application of the Ti-in-quartz thermobarometer in V1, V2, and V3 veins. The absence of rutile in V4 veins implies a TiO_2 activity less than one, therefore the Ti-in-quartz thermobarometer is not applied in V4.

Fluid inclusion bulk compositions are remarkably similar throughout the evolution of the hydrothermal system (Table 5), however, pressures and temperatures of vein formation changed throughout, trapping these fluids under different conditions. Fluid salinities remained consistently low (~3–6 wt % NaCl equiv) and CO_2 concentrations (~5–10 mol %) also changed little. Three-phase, CO_2-bearing, primary fluid inclusions are similar in composition to two-phase primary fluid inclusions, but contain more CO_2. Three-phase inclusions are scattered within and among two-phase inclusions and petrographic observations and CL images show no evidence for successive entrapment of these two types of inclusions. We infer that the fluid inclusion types represent the same fluids, with variations in CO_2 concentration, due to variations in input fluid, pressure, or CO_2 degassing.

B35 inclusions dominate Q1 in V1 and V2 veins. B45 inclusions are most abundant in Q1 in V3 veins, and B20 inclusions dominate Q1 in V4 veins. We therefore calculated isochores from the dominant inclusion types from each vein stage to estimate pressure and temperature conditions of vein formation.

Intersections of fluid inclusion isochores with Ti-in-quartz isopleths suggest vein formation conditions of around 2.7 ± 0.2 kbars and 650° ± 40°C for V1 veins, around 1.9 ± 0.2 kbars and 530° ± 40°C for V2 veins, and around 0.65 ± 0.15 kbars and 400° ± 40°C for V3 veins (Fig. 15). We infer that the pressures and depths of formation for V3 veins provide the upper depth limit for V4 veins, and the fluid inclusion homogenization temperatures and pressures constrain the lower limits of vein-forming conditions. Taking their spatial distribution into consideration, the estimated pressure and temperature conditions are around 0.40 to 0.65 kbars and 250° to 300°C for V4 veins.

The pressure and temperature conditions of the formation of V1 veins are just below the water-saturated solidus of granite (Holtz et al., 2001) and are in the typical range for the emplacement of porphyritic dikes that initiate these hydrothermal systems (Naney, 1983; Dilles, 1987). V1 veins therefore formed at conditions very close to those of the crystalizing magma from which the fluids were exsolved, and the fluids trapped in these inclusions are the earliest recognized magmatic-hydrothermal fluids. At such high pressures and temperatures, quartz solubility is very high (Fig. 16) and is sensitive to decreases in both pressure and temperature. The high quartz solubility in this pressure and temperature range explains the quartz-dominated veins that are commonly early and deep in most porphyry systems, including Dabaoshan. In many porphyry systems, CL textures reveal rounded CL-bright quartz cores overgrown by CL-dark quartz with euhedral growth zones (Rusk and Reed, 2002; Landtwing et al., 2005; Müller et al., 2010; Maydagán et al., 2015). This texture is interpreted to form from the cooling of fluid through the zone of retrograde quartz solubility at constant or slightly decreasing pressure. In these deposits, this texture and cooling path were inferred to result in Fe and Cu-Fe sulfide mineralization. Although the dissolution texture was recognized at Dabaoshan, its rare occurrence suggests that retrograde quartz dissolution rarely occurred in the Dabaoshan hydrothermal system. Instead, the transition from V2 to V3 veins likely followed the path illustrated in Figure 16. As a result of the high pressures of vein formation, the fluids that formed the Dabaoshan deposit hardly passed through the zone of retrograde quartz solubility. The large predicted change in quartz solubility from V2 to V3 veins, from ~5,000 to ~1,300 mg/kg explains why quartz is more abundant in V3 veins compared to D veins in other porphyry-type ore deposits, which characteristically contain very little quartz (Gustafson and Hunt, 1975; Muntean and Einaudi, 2001; Catchpole et al., 2015).

Hydrologic regime and depths of vein formation

The pressure of vein formation is a function of both depth and hydrologic regime (Seedorff et al., 2005). Under lithostatic conditions, pressure is defined by the mass of the overlying rock, whereas under hydrostatic conditions, pressure is defined by the mass of the overlying water column. Hydrostatic conditions imply an open fracture network from the surface downward, through which hydrothermal fluids flow. Under lithostatic conditions however, plastic deformation of the rock causes fractures to seal quickly such that open space for fluid flow is not maintained. The transition between brittle and ductile behavior is generally inferred to occur around 400°C. This temperature may increase as strain rate increases (Fournier, 1999). Transient superlithostatic pressures may be achieved prior to failure of the rock where fluid pressures are higher than the surrounding rock (Carrigan et al., 1992).

A transition in the hydrologic regime from lithostatic pressure to hydrostatic pressure in porphyry systems was originally proposed by Gustafson and Hunt (1975) to account for the change in the structure and style of veins in the El Salvador porphyry copper deposit. Muntean and Einaudi (2000) infered that A veinlets formed under lithostatic pressure at temperatures of 600° to 700°C when the host rock was still ductile, while banded quartz veinlets formed after adiabatic decompression to hydrostatic pressure at temperatures <350°C, in the porphyry gold deposits of the Refugio district.

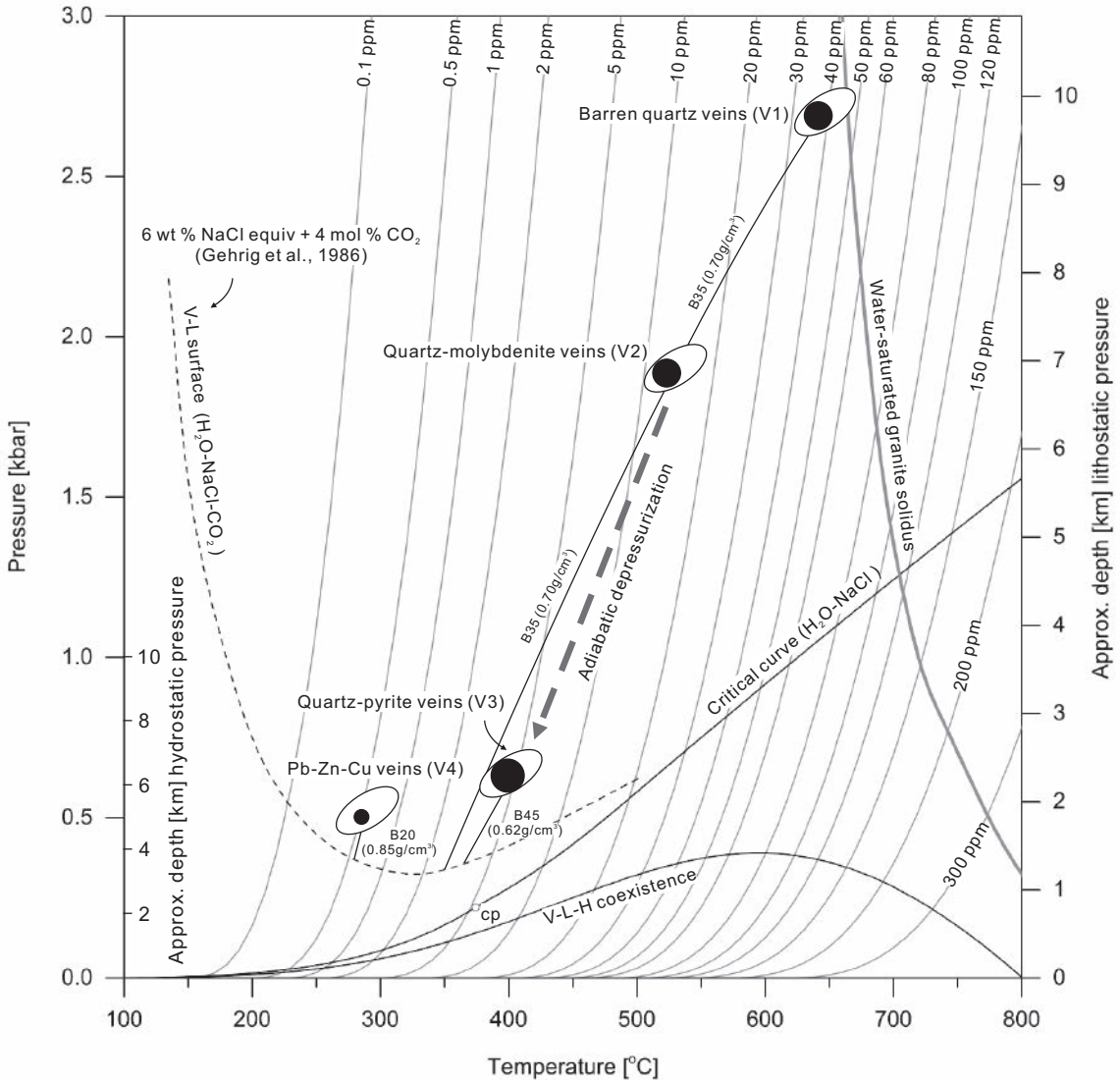

Fig. 15. Pressure-temperature diagram showing the formation conditions of quartz-bearing veins in Dabaoshan. Pressure and temperature data of solvi in H_2O-NaCl system are from Driesner and Heinrich (2007). Critical curve for the H_2O-NaCl-CO_2 system with 4 mol % CO_2 and salinity of 6 wt % NaCl equiv is from Gehrig et al. (1986). Water-saturated granite solidus is from Holtz et al. (2001). Selected Ti isopleths are illustrated in Figure 15 instead of using the specific Ti isopleths corresponding to each vein generations for better demonstration.

V1 and V2 veins in Dabaoshan are inferred to have formed at pressures between 1.9 and 2.7 kbars, and at temperatures between 500° and 650°C. Under such conditions, the host rock and the veins (Fig. 3A, C) are ductile and fractures should seal rapidly such that open space is not expected. V3 veins are estimated to have formed as fluids cooled to less than 400°C under transient excursions to hydrostatic pressure. V4 veins on the other hand formed at temperatures less than 300°C at pressures similar to and lower than V3 veins under conditions where brittle behavior of the rocks is much more consistent. Therefore, our estimations of pressure and temperature support the conclusion that early quartz-bearing veins, characterized by granular (or sugary) mosaics of CL-bright and homogeneous textures formed under dominantly lithostatic pressure, while late quartz-bearing pyrite and base metal veins characterized by CL-dark quartz with euhedral growth zonations crystalized under dominantly hydrostatic conditions.

The pressure estimations of ~2.7 kbars for V1 veins and ~1.9 kbars for V2 veins imply depths of vein formation at about 9.8 ± 0.7 and 6.9 ± 0.7 km (Figs. 15, 17), respectively, under lithostatic load assuming crustal density of 2.75 g/cm^3. Thus, there is an apparent change in depth of roughly 3 km between V1 and V2 veins, even though they are quite similar in mineral content, CL texture, deposit-scale distribution, and fluid inclusion characteristics. They are however distinct in Ti concentration. Such a change in depth, during the early formation of a porphyry deposit, accompanied by only a roughly 100°C drop in temperature is unlikely, especially since the veins largely overlap in space. The wavy vein walls of some V1 veins suggest they formed when the host rock was still hot and ductile. Under such conditions, fluid accumulated at the

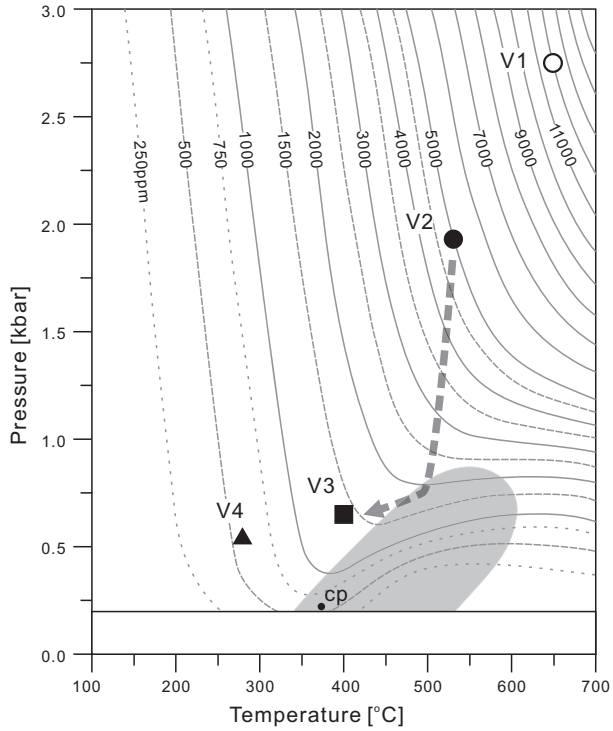

Fig. 16. Quartz solubility in water as function of pressure and temperature. Data calculated with the computer program SUPCRT92 (Johnson et al., 1992). Calculation was conducted in equilibrium between quartz and pure water. The shaded area marks a region of retrograde solubility in which the solubility increases with decreasing temperature at a constant pressure. See text for discussion.

top of the magma chamber may propagate upward through fractures with minimal loss of pressure owing to the low density of the fluid (Carrigan et al., 1992). Thus, fluid overpressure in and directly above the carapace of a magma chamber may lead to overestimated pressures. We infer that the actual depth of V1 vein formation may be overestimated as a result and is likely slightly deeper than or similar to V2 veins (Figs. 15, 17), and the calculated depth of 9.8 km may indicate the depth of the top of the magma chamber from which this fluid emanated.

The permeability of the brittle crust is capable of maintaining hydrostatic pressure to a depth of 10 km or more over the times scales of 10 to 1,000 yrs (Townend and Zoback, 2000). Locations exhibiting near-hydrostatic fluid pressures at great depths in the range of 5 to over 12 km have been reported in Dixie Valley, Nevada (5–7 km, Hickman et al., 1997), Soultz HDR, France (5 km, Baumgärtner et al., 1998), Siljian, Sweden (7 km, Lund and Zoback, 1999), KTB, Germany (9.1 km, Huenges et al., 1997), and Kola, Russia (12.2 km, Borevsky et al., 1987). The estimated pressure of ~0.65 ± 0.15 kbars for V3 veins is equivalent to a depth of 6.5 km under hydrostatic pressure assuming fluid density of 1 g/cm^3, close to the inferred depths of V2 vein formation (Figs. 15, 17). Hydrostatic pressures at this depth may have been transient, where quartz-dominated veins formed when the system was sealed and under lithostatic load, but when brittle failure occurred and fluids moved upward and cooled to form pyrite veins with muscovite alteration. An upper depth limit of ~6 km is inferred for V4 veins based on their spatial distribution.

Validity of pressure and temperature estimates

The accidental analysis of rutile needles during laser ablation may lead to estimations of Ti concentrations in quartz that are higher than the true values. This would, in turn, cause the overestimation of pressure and temperature conditions for V1, V2, and V3 veins. However, great effort was paid to avoid and remove the contamination of Ti from rutile needles during the selection of laser ablation spots and the data reduction process. Further, as shown in Figure 8, results from within individual veins, and across multiple veins of the same type have consistent Ti concentrations. If falsely high Ti concentrations were caused by the accidental analysis of rutile needles, we would expect a wider range of Ti concentration within and among samples of the same vein type (Table 2). A growing number of studies consistently demonstrate that Ti concentrations in quartz-bearing veins from the porphyry deposits range from <1 up to ~200 ppm (Landtwing and Pettke, 2005; Rusk, 2006, 2012; Müller et al., 2010; Maydagán et al., 2015). Comparisons between microprobe and LA-ICP-MS analyses on the same samples show general agreement in Ti concentrations, within a few percent between the two analytical techniques, demonstrating that contamination from accidental rutile analysis can be avoided by careful analytical techniques (Donovan et al., 2011; Audétat et al., 2015). Furthermore, the correlation between CL intensity and Ti concentration among all quartz generations is consistent with Ti incorporation into the quartz. Numerous studies of igneous, metamorphic, and hydrothermal quartz have shown that CL intensity correlates closely with Ti concentration in quartz (Larsen et al., 2004; Wark et al., 2007; Rusk et al., 2008b; Leeman et al., 2012; Müller et al., 2012; Rusk, 2012; Audétat, 2013; Müller and Knies, 2013; Maydagán et al., 2015; Mercer et al., 2015). If the Ti analyses here and in all of the above studies were the result of accidental analysis of nanoinclusions of rutile, then the quartz CL intensity should not correlate to Ti concentration and also should not decrease from vein to vein generation.

The lack of the critical homogenization behavior and the low homogenization temperatures of the two-phase fluid inclusions in V1 and V2 veins indicate high fluid densities relative to "intermediate density fluids" in many other porphyry-type deposits (e.g., Bingham Canyon, Utah: Redmond et al., 2004; El Teniente, Chile: Klemm et al., 2007; Questa, New Mexico: Klemm et al., 2008; Butte, Montana: Rusk et al., 2008a; Morococha district, Peru: Catchpole et al., 2015; Altar, Argentina: Maydagán et al., 2015). Even if Ti concentrations in V1 are slightly overestimated, the slopes of the isochores still require pressures over 2 kbars, even for Ti concentrations as low as 10 to 20 ppm (as for V2 veins). We infer that they are more likely to be slightly underestimated, if anything, due to minor incorporation of later CL-dark Ti-deficient Q2. Therefore, the slope of the isochores, combined with geologically reasonable estimates of temperature, still require pressures in around 2 kbars or more for the formation of V1 and V2 veins. Based on similarities with quartz Ti concentrations in veins in other porphyry deposits, and on the observed correlation between CL intensity and Ti concentration in the Dabaoshan veins, we infer that contamination of Ti from the

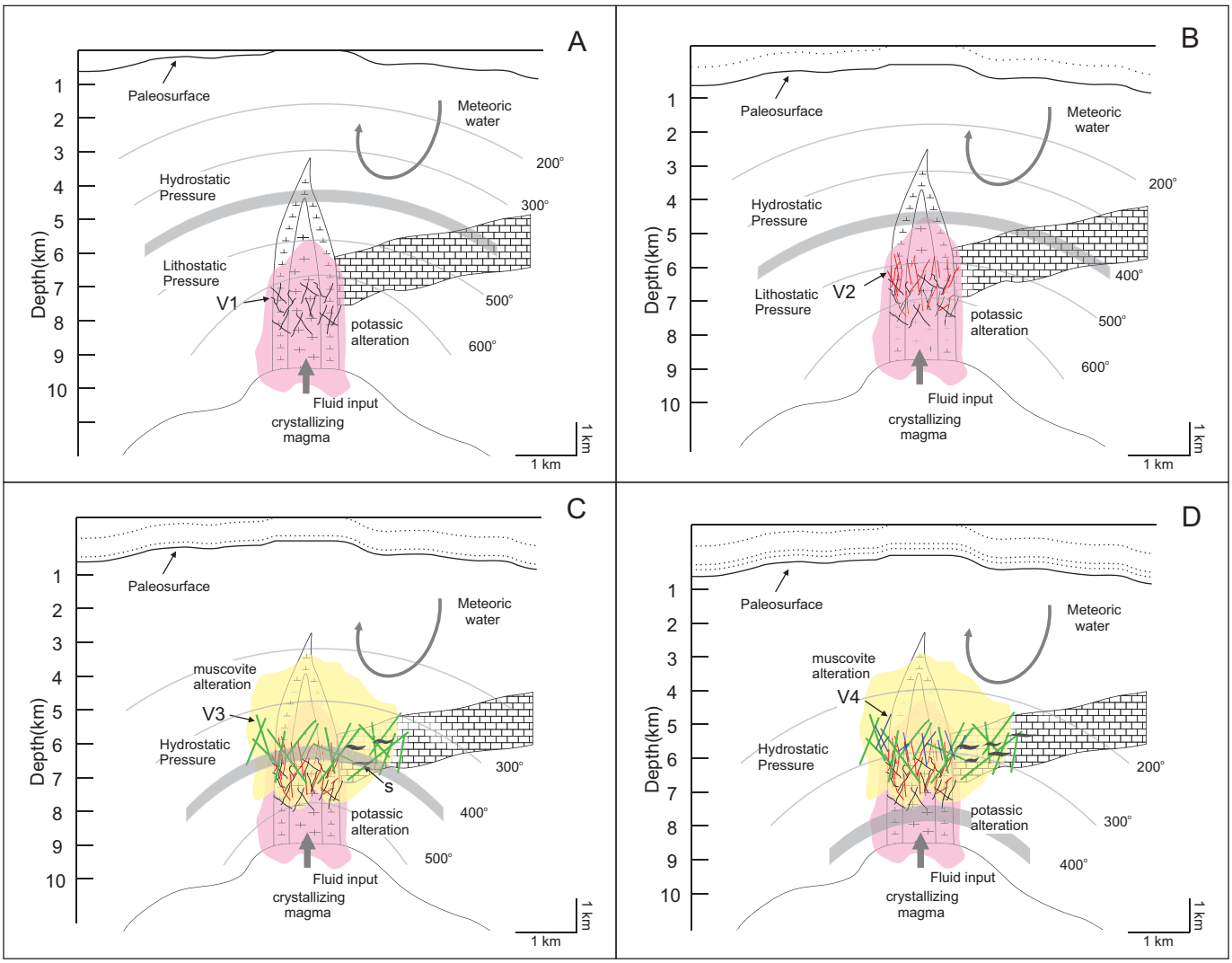

Fig. 17. Schematic diagram showing the evolution of the magmatic-hydrothermal system at Dabaoshan. A. As crystallization progressed in the magma chamber beneath the mineralization zone, low-salinity magmatic fluid continuously exsolved and accumulated at the top of the magma chamber. V1 veins accompanied by K-feldspar alteration formed when magmatic fluid was driven into fractures by overpressurization. B. V2 veins formed when the magmatic fluid cooled to around 530°C at depths about 6.9 km. C. The hydrologic regime switched from lithostatic pressure to hydrostatic pressure at about 400°C. V3 veins started to form with muscovite alteration. Outward migration of the hydrothermal fluid interacted with the Devonian limestone and formed the strata-bound mineralization. D. V4 veins formed at shallower depths as the magmatic-hydrothermal system cooled to around 250° to 300°C and fluid propagated outward. See text for discussion.

rutile needles to our data is negligible. The calculated pressure and temperature conditions for V1, V2, and V3 veins are therefore reliable to the extent that the isochores and Ti-in-quartz isopleths are reliable.

Rapid quartz precipitation could also lead to excess incorporation of Ti into the quartz structure (e.g., Martin and Armington, 1983; Armington and Larkin, 1985; Armington, 1991; Watson and Liang, 1995; Watson, 1996, 2004; Jourdan et al., 2009; Huang and Audétat, 2012), and could lead to the overestimation of pressure and temperature conditions by the intersection of fluid inclusion isochores. If this occurred at Dabaoshan, disequilibrium incorporation of trace elements as a result of rapid precipitation should incorporate all trace elements at unusually high levels with respect to quartz precipitated at lower rates. The positive correlation and increased concentration of trace elements in some strongly zoned V4 quartz crystals likely reflects disequilibrium incorporation of trace elements into the quartz structure (e.g., Figs. 7E, 8, 18). Euhedral growth zones in V4 veins display thin growth bands, indicating fluctuations of the physical and/or chemical conditions of quartz precipitation. However, V1 and V2 veins show no correlations between any trace elements, and Al, Li, and Ge concentrations are significantly lower than in other vein types (Fig. 8). This suggests that disequilibrium incorporation of trace elements has not likely led to significant excess Ti concentration in these early veins.

Unusually great depth of ore deposit formation

Our results indicate that the earliest quartz-bearing veins in Dabaoshan porphyry Mo deposit formed at pressures up to

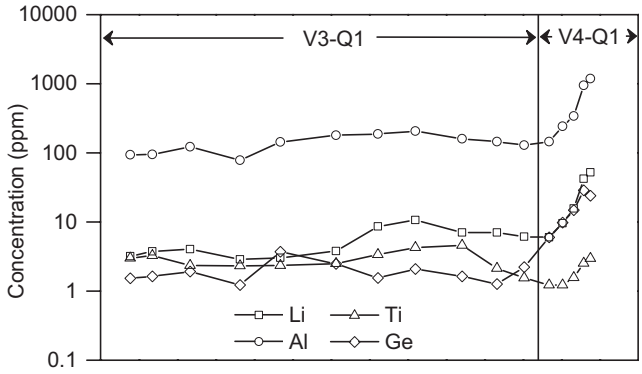

Fig. 18. Trace element concentration profile of a quartz crystal; corresponding SEM-CL image and laser ablation spots are marked in Figure 7E. Five spots on the right are from V4-Q1 and the rest are from V3-Q1. Same data are also plotted as green squares and triangles in Figure 8.

~2.7 kbars. These are the highest pressures reported for any porphyry-type deposit, making it potentially the deepest porphyry deposit studied to date.

A number of lines of evidence support our conclusion that the Dabaoshan porphyry deposit formed at greater depths than other porphyry deposits. The pressures over which veins form are reflected in fluid inclusion phase relationships. Coexisting halite-bearing fluid inclusions and vapor-rich fluid inclusions are abundant in most porphyry deposits, and result from the immiscibility of a single-phase H_2O-NaCl (-CO_2) hydrothermal fluid over much of the pressure and temperature range that coincides with the formation of many porphyry-type ore deposits (Gustafson and Hunt, 1975; Bodnar et al., 1985, 2014; Hedenquist et al., 1998; Heinrich et al., 1999). At Dabaoshan however, only a few halite-bearing fluid inclusions were identified out of thousands of fluid inclusions observed (Fig. 11P). The general lack of such inclusions at Dabaoshan indicates that it was extremely rare for the pressure of vein formation to drop below the solvus to the pressures required for fluid unmixing. The near absence of halite-bearing and vapor-rich fluid inclusions coupled with an abundance of low-salinity, CO_2-rich fluid inclusions were also observed in the White Pine Fork molybdenum prospect, the depth of which was estimated by geologic reconstruction to be ~7 km below surface (John, 1989), and in the Trout Lake Mo deposit, British Columbia, where fluid trapping conditions were inferred to be above the two-phase region of the H_2O-NaCl-CO_2 system (Linnen and Williams-Jones, 1990).

Fluid inclusions trapping a low-salinity (~1–6 wt % NaCl equiv) single-phase supercritical fluid have been recognized in deep quartz-rich veins from several porphyry deposits (e.g., Bingham Canyon, Utah: Redmond et al., 2004; El Teniente, Chile: Klemm et al., 2007; Questa, New Mexico: Klemm et al., 2008; Butte, Montana: Rusk et al., 2008a; Rosia Poieni, Romania: Kouzmanov et al., 2010; Morococha district, Peru: Catchpole et al., 2015; Altar, Argentina: Maydagán et al., 2015). Figures 15, 19, 20 and 21 show that pressure of each generation of quartz-bearing vein at Dabaoshan is higher than the corresponding V-L surface, therefore, fluid unmixing rarely occurred during the formation of this deposit and the low- to moderate-salinity parental magmatic fluid dominated throughout the life of the hydrothermal system.

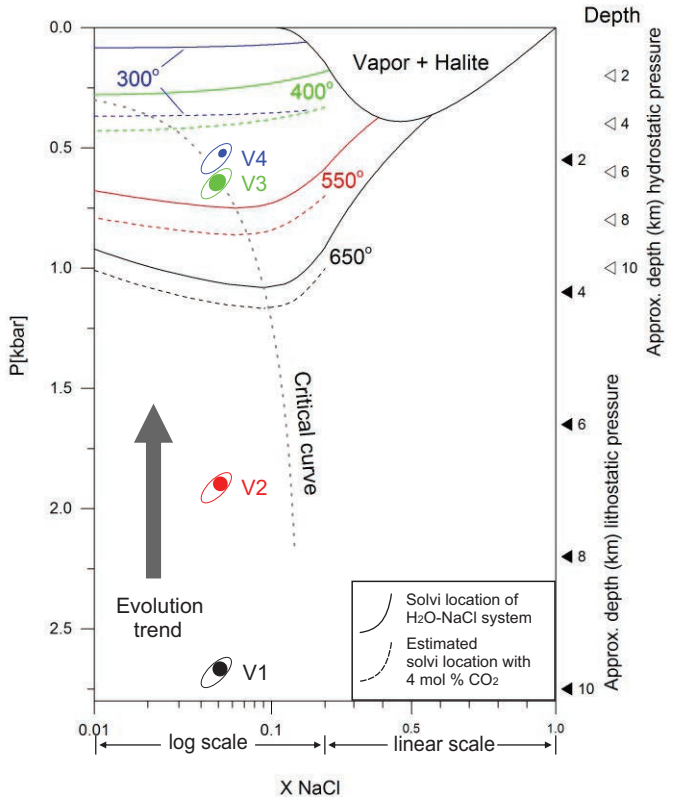

Fig. 19. P-X diagram showing the positions of solvi in H_2O-NaCl system and estimated positions of solvi in H_2O-NaCl-CO_2 system with 4 mol % CO_2. Pressure and temperature data of solvi in H_2O-NaCl system are from Driesner and Heinrich (2007). Estimated solvi in H_2O-NaCl-CO_2 system are extrapolated from Gehrig et al. (1986). The presence of 4 mol % CO_2 increases the pressure of solvus by about 0.175 kbars at 300°C, 0.150 kbars at 400°C, 0.113 kbars at 550°C, and 0.0875 kbars at 650°C. Filled triangles on the right-hand side refer to depths calculated from lithostatic pressure, and the open triangles refer to depths calculated from hydrostatic pressure.

The great depths of formation are consistent with the lack of Jurassic eruptive rocks and the large total area of the exposed granodiorite and granodiorite porphyry in the Dabaoshan district, which also indicates relatively deep erosion levels and thus deep emplacement of ore-forming porphyries and the associated hydrothermal system. Lastly, as discussed above, the rare occurrence of quartz dissolution via cooling through the zone of retrograde quartz solubility, combined with the quartz-rich nature of pyrite veins with muscovite alteration is also consistent with unusually high pressures, greater than is typical at other porphyry-type deposits, where retrograde quartz solubility has been identified (e.g., Grasberg, Indonesia: Penniston-Dorland, 2001; Butte, Montana: Rusk and Reed, 2002; Bingham Canyon, Utah: Landtwing and Pettke, 2005; Oyu Tolgoi, Mongolia: Müller et al., 2010; Altar, Argentina: Maydagán et al., 2015).

Relationship between porphyry and strata-bound base metal mineralization at Dabaoshan

The limestone-hosted strata-bound Cu-Pb-Zn deposit has been classified by some as a Devonian volcanic-associated massive sulfide deposit because orebodies occur as stratiform lenses and they are generally conformable with the limestone

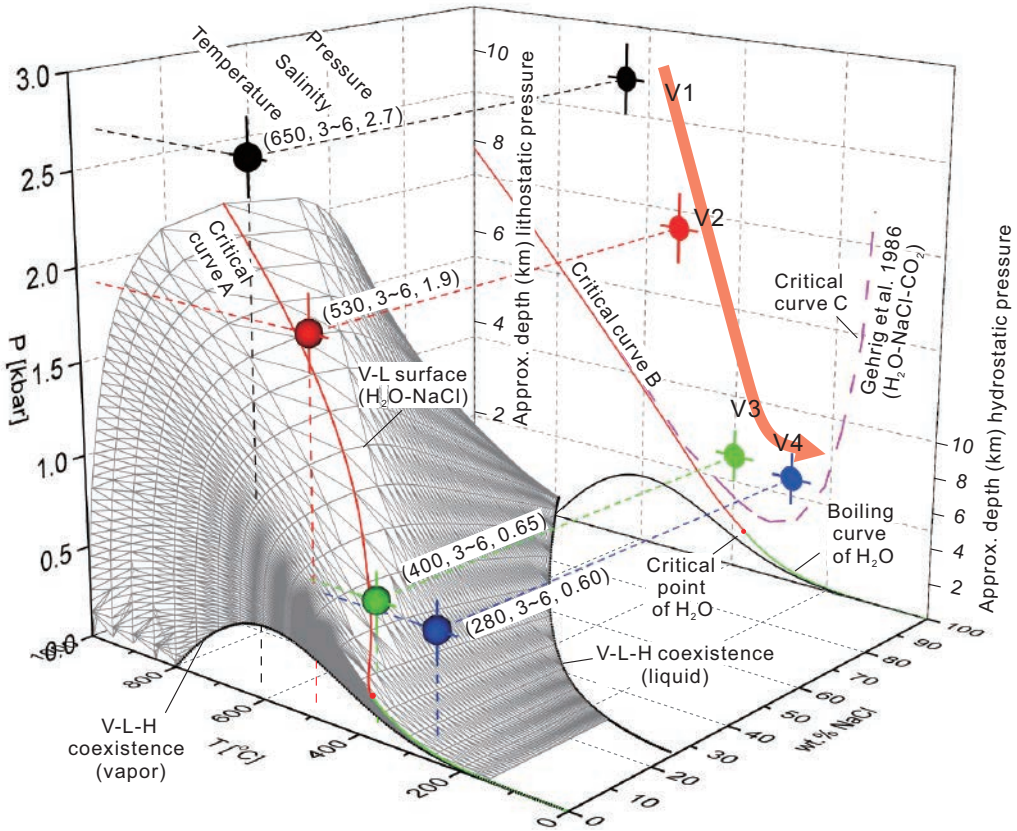

Fig. 20. Three-dimensional diagram and pressure-temperature projection showing the evolution history of the Dabaoshan porphyry Mo system. Data constructing the frame of H_2O-NaCl system are from Driesner and Heinrich (2007). The crest of the V-L surface consists of the boiling curve of pure water and the critical curve of the H_2O-NaCl system (critical curve A). Critical curve B is the P-T projection of critical curve A. The critical curve of the H_2O-NaCl-CO_2 system with 6 wt % NaCl equiv and 4 mol % CO_2 (Gehrig et al., 1986) is plotted in the pressure-temperature projection (critical curve C). Average temperature, salinity, and pressure of each generation of veins are plotted with error bars showing the variation of pressure and temperature. Approximate depths calculated from lithostatic and hydrostatic pressures are labeled, assuming upper crust density of 2.75 g/cm^3 and water density of 1.0 g/cm^3.

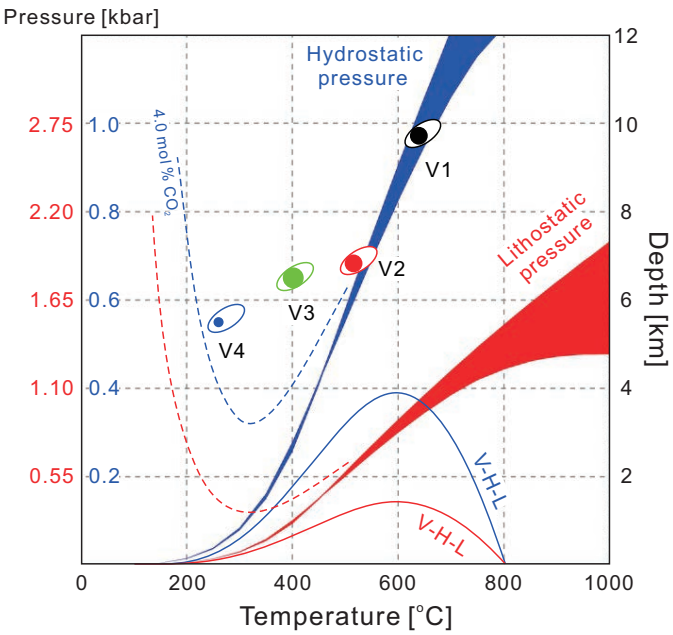

layers (Ge and Han, 1986; Yao and Zeng, 1994; Yang, 1997). Others argue that there is a genetic relationship between the strata-bound deposit and the Jurassic porphyry system, as suggested by their intimate spatial relationship (Liu et al., 1985; Huang et al., 1987; Xu et al., 2008; L. Wang et al., 2011). Although the relationship between the porphyry mineralization and the strata-bound mineralization was not the key focus of our study, we studied several samples from the strata-bound deposits and our results have implications for the genetic links between porphyry and strata-bound mineralization.

Skarn mineralization is developed along the contact zone between the Dabaoshan dacite porphyry and the limestone, and V3 veins clearly extend from the porphyries into the strata-bound deposit, demonstrating interaction between porphyry-related hydrothermal fluids and the Donggangling limestone.

Fig. 21. Depth-temperature diagram showing the interpreted sequence of emplacement of quartz-bearing veins. Red and blue symbols illustrate lithostatic and hydrostatic conditions, respectively. Red and blue ribbons represent the V-L surface corresponding to salinity range of 2 to 12 wt % NaCl equiv under lithostatic and hydrostatic pressure conditions, respectively.

The presence of chalcopyrite daughter minerals in some fluid inclusions in Jurassic porphyry-related veins indicates that the hydrothermal fluid contained significant Cu. Bulk analysis of fluid inclusion in quartz from the Dabaoshan porphyry system suggest an average concentration of 0.04 g/L Cu, 0.2 g/L Pb, and 0.1 g/L Zn in hydrothermal fluid (Cai and Liu, 1993b), showing its potential for Cu, Pb, and Zn mineralization. Average $\delta^{34}S$ values around 0‰ support a dominantly magmatic source of S for sulfides both in the strata-bound deposit and the V1 to V4 veins. This signature is clearly different from that in disseminated pyrite in the upper Devonian Tianziling limestone, which ranges from +8.7 to +17.9‰, or in the Middle Devonian Dongangling limestone, which ranges from –22.5 to –5.2‰ (Xu et al., 2008).

Similarly H and O isotopes suggest a magmatic source for fluids in both porphyry-hosted and strata-bound mineralization (Table 6). Using temperatures derived from fluid inclusions and quartz trace elements, recalculated $\delta^{18}O$ values for water varies from ~10.5‰ in V2 veins to ~9.7‰ in V3 veins to ~8.1‰ in VS veins. Almost all the δD-$\delta^{18}O$ data lie in the range of primary magmatic water (Fig. 14), indicating that both the porphyry Mo deposit and the strata-bound Cu-Pb-Zn deposit have a magmatic source of hydrothermal fluid.

CL textures and trace elements in the VS quartz are similar to V3 and V4 veins (Fig. 7). The texture of euhedral growth zones of oscillating CL intensity and sector zoning is characteristic in porphyry systems (e.g., Penniston-Dorland, 2001; Rusk and Reed, 2002; Landtwing et al., 2005; Müller et al., 2010; Maydagán et al., 2015) but has not been reported in SEDEX- or VMS-type deposits. Trace element concentrations of VS quartz consistently lie in the range between V3 and V4 veins, consistent with fluids of similar compositions and similar pressure and temperature conditions (Fig. 8). Lastly, CO_2-rich fluid inclusions are rare in SEDEX- or VMS-type deposits (e.g., Wilkins, 1977; Cazañas et al., 2008), and the high CO_2 concentrations in fluid inclusions in VS quartz (Fig. 11M-Q) were likely generated by the reaction between the acidic hydrothermal fluid and the limestone. Based on all of the above lines of evidence, we infer that there was a significant contribution to the strata-bound Cu-Pb-Zn deposit from the porphyry system. The absence of fluid unmixing resulted from the unusually great depths in the Dabaoshan porphyry system likely inhibited significant Cu precipitation within the porphyry system. Copper in the hydrothermal fluid therefore moved laterally outward and precipitated after the acidic hydrothermal fluid interacted with the Devonian limestone (Fig. 17). The abundant CO_2 in the VS quartz (~48–66 mol %) likely resulted from the interaction between the acidic hydrothermal fluid and the Devonian limestone.

Conclusions

Fluid inclusion petrography and microthermometry reveal that the Dabaoshan porphyry Mo deposit formed from a continuous supply of low-salinity, CO_2-bearing ore-forming fluid derived from a crystalizing magma chamber. Barren quartz and quartz-molybdenite veins formed under lithostatic pressure and are comprised of CL-bright granular mosaics of quartz, whereas quartz-pyrite veins, base metal veins, and strata-bound mineralization, formed under hydrostatic pressure, are composed of CL-dark quartz of euhedral growth zone of oscillating CL intensity. CL intensity decreases in each successive vein type, corresponding to the decrease of quartz Ti concentrations, resulting from decreasing temperatures of the hydrothermal system.

The corrected pressure and temperature conditions of the hydrothermal fluid in Dabaoshan consistently lie above the V-L surface of the H_2O-NaCl-CO_2 system, so fluid unmixing rarely occurred to form halite-bearing and vapor-rich fluid inclusions, which are characteristic of most porphyry-type ore deposits. Estimated depth for the mineralization zone is 6 to 7 km, which is much greater than typical porphyry deposits.

Quartz CL textures, trace elements, sulfur isotope compositions of sulfides, as well as H and O isotope compositions of water clearly demonstrate the significant contribution from the porphyry system to the strata-bound Cu-Pb-Zn mineralization. The great depth of formation and lack of fluid unmixing may have allowed Cu to stay in solution and move upward and outward into the surrounding limestone where it precipitated as strata-bound Cu-Pb-Zn mineralization.

Acknowledgments

This research was financially supported by the National Basic Research Program of China (973 Program) granted 2012CB416705, the One Hundred Person Project of the Chinese Academy of Sciences, and the Advanced Geoscience Investigations LLC. We acknowledge our thanks to Pete Stelling, Charles Wandler, and Yongmei Zhang, who helped to carry out experiments at Western Washington University. We thank David Cooke for the constructive editorial reviews that led to significant improvement of the manuscript. We also thank Stuart Simmons, Lijuan Ying, and an anonymous reviewer for their useful insights that improved the manuscript. We thank Hong Zhong for helpful discussions.

REFERENCES

Armington, A.F., 1991, Recent advances in the growth of high quality quartz: Progress in Crystal Growth and Characterization of Materials, v. 21, p. 97–111.

Armington, A.F., and Larkin, J.J., 1985, The growth of high-purity, low dislocation quartz: Journal of Crystal Growth, v. 71, p. 799–802.

Audétat, A., 2013, Origin of Ti-rich rims in quartz phenocrysts from the Upper Bandelier tuff and the Tunnel Spring tuff, southwestern USA: Chemical Geology, v. 360–361, p. 99–104.

Audétat, A., and Günther, D., 1999, Mobility and H_2O loss from fluid inclusions in natural quartz crystals: Contributions to Mineralogy and Petrology, v. 137, p. 1–14.

Audétat, A., Garbe-Schönberg, D., Kronz, A., Pettke, T., Rusk, B., Donovan, J.J., and Lowers, H.A., 2015, Characterisation of a natural quartz crystal as a reference material for microanalytical determination of Ti, Al, Li, Fe, Mn, Ga and Ge: Geostandards and Geoanalytical Research, v. 39, p. 171–184.

Bakker, R.J., 1997, Clathrates: Computer programs to calculate fluid inclusion V-X properties using clathrate melting temperatures: Computers and Geosciences, v. 21, p. 1–18.

Baumgärtner, J., Gérard, A., Baria, R., Jung, R., Tran-Viet, T., Gandy, T., Aquilina, L., and Garnish, J., 1998, Circulating the HDR reservoir at Soultz: Maintaining production and injection flow in complete balance: Geothermal Reservoir Engineering Workshop, 23rd, Stanford, Stanford University, Proceedings, p. 11–20.

Bodnar, R.J., and Vityk, M.O., 1994, Interpretation of microthermometric data for H_2O-NaCl fluid inclusions, *in* De Vivo, B., and Frezzotti, M.L., eds., Fluid inclusions in minerals: Methods and applications: Blacksburg, VA, Virginia Technical Institute, p. 117–130.

Bodnar, R.J., Burnham, C.W., and Sterner, S.M., 1985, Synthetic fluid inclusions in natural quartz. III. Determination of phase equilibrium properties in the system H_2O-NaCl to 1000°C and 1500 bars: Geochimica et Cosmochimica Acta, v. 49, p. 1861–1873.

Bodnar, R.J., Lecumberri-Sanchez, P., Moncada, D., and Steele-MacInnis, M., 2014, Fluid inclusions in hydrothermal ore deposits: Treatise on Geochemistry, v. 13, p. 119–142.

Borevsky, L.V., Vartanyan, G.S., and Kulikov, T.B., 1987, Hydrogeological essay, *in* Kozlovsky, Y. A. ed., The superdeep well of the Kola penisula: New York, Springer, p. 271–287.

Bowers, T.S., and Helgeson, H.C., 1983, Calculation of the thermodynamic and geochemical consequences of nonideal mixing in the system H_2O-CO_2-NaCl on phase relations in geologic systems: American Mineralogist, v. 68, p. 1059–1075.

Breiter, K., Ackerman, L., Svojtka, M., and Müller, A., 2013, Behavior of trace elements in quartz from plutons of different geochemical signature: A case study from the Bohemian Massif, Czech Republic: Lithos, v. 175–176, p. 54–67.

Brimhall, G.H., Jr., 1977, Early fracture-controlled disseminated mineralization at Butte, Montana: Economic Geology, v. 72, p. 37–59.

Burnham, C.W., 1967, Hydrothermal fluids at the magmatic stage, *in* Barnes, H.L., ed., Geochemistry of hydrothermal ore deposits: New York, Holt Rinehart and Winston, p. 34–76.

Cai, J., and Liu, J., 1993a, The age of the magmatic rocks of Dabaoshan polymetallic ore field in north Guangdong: Guangdong Geology, v. 8, p. 45–52 (in Chinese with English abs.).

——1993b, Research and its application on the inclusions characteristics in the Dabaoshan polymetallic deposit, northern Guangdong: Journal of Mineralogy and Petrology, v. 13, p. 33–40 (in Chinese with English abs.).

Carrigan, C.R., Schubert, G., and Eichelberger, J.C., 1992, Thermal and dynamical regimes of single- and two-phase magmatic flow in dikes: Journal of Geophysical Research, v. 97, p. 17,377–17,392.

Catchpole, H., Kouzmanov, K., Putlitz, B., Seo, J.H., and Fontbote, L., 2015, Zoned base metal mineralization in a porphyry system: Origin and evolution of mineralizing fluids in the Morococha district, Peru: Economic Geology, v. 110, p. 39–71.

Cazañas, X., Alfonso, P., Melgarejo, J.C., Proenza, J.A., and Fallick, A.E., 2008, Geology, fluid inclusion and sulphur isotope characteristics of the El Cobre VHMS deposit, southern Cuba: Mineralium Deposita, v. 43, p. 805–824.

Chen, C.H., Lee, C.Y., and Shinjo, R., 2008, Was there Jurassic paleo-Pacific subduction in South China?: Constraints from $^{40}Ar/^{39}Ar$ dating, elemental and Sr-Nd-Pb isotopic geochemistry of the Mesozoic basalts: Lithos, v. 106, p. 83–92.

Chen, K., Cai, J., Liu, L., Li, Y., Fu, T., Hu, M., Wang, L., Yang, Z., Xu, B., Xia, J., and Zhang, W., 2009, Comprehensive metallogeny research of the Dabaoshan polymetallic deposit, Shaoguan, Guangdong, Wuhan Geological Survey Center of China Geological Survey: Internal Report (in Chinese).

Clayton, R.N., Mayeda, T.K., and Oneil, J.R., 1972, Oxygen isotope-exchange between quartz and water: Journal of Geophysical Research, v. 77, p. 3057–3067.

Diamond, L.W., Tarantola, A, and Stünitz, H., 2010, Modification of fluid inclusions in quartz by deviatoric stress. II: Experimentally induced changes in inclusion volume and composition: Contributions to Mineralogy and Petrology, v. 160, p. 845–864.

Dilles, J.H., 1987, Petrology of the Yerington batholith, Nevada: Evidence for evolution of porphyry copper ore fluids: Economic Geology, v. 82, p. 1750–1789.

Dilles, J.H., Einaudi, M.T., Proffett, J., and Barton, M.D., 2000, Overview of the Yerington porphyry copper district: Magmatic to nonmagmatic sources of hydrothermal fluids: Their flow paths and alteration effects on rocks and Cu-Mo-Fe-Au ores: Society of Economic Geologists Guidebook Series, v. 32, p. 55–66.

Donovan, J.J., Lowers, H.A., and Rusk, B.G., 2011, Improved electron probe microanalysis of trace elements in quartz: American Mineralogist, v. 96, p. 274–282.

Driesner, T., and Heinrich, C.A., 2007, The system H_2O-NaCl. Part I: Correlation formulae for phase relations in temperature-pressure-composition space from 0 to 1000°C, 0 to 5000 bar, and 0 to 1 X_{NaCl}: Geochimica et Cosmochimica Acta, v. 71, p. 4880–4901.

Duan, Z., Møller, N., and Weare, J.H., 1992a, An equation of state for the CH_4-CO_2-H_2O system: I. Pure systems from 0 to 1000°C and 0 to 8000 bar: Geochimica et Cosmochimica Acta, v. 56, p. 2605–2617.

——1992b, An equation of state for the CH_4-CO_2-H_2O system: II. Mixtures from 50 to 1000°C and 0 to 1000 bar: Geochimica et Cosmochimica Acta, v. 56, p. 2619–2631.

Flem, B., Larsen, R.B., Grimstvedt, A., and Mansfeld, J., 2002, In situ analysis of trace elements in quartz by using laser ablation inductively coupled plasma mass spectrometry: Chemical Geology, v. 182, p. 237–247.

Fournier, R.O., 1999, Hydrothermal processes related to movement of fluid from plastic into brittle rock in the magmatic-epithermal environment: Economic Geology, v. 94, p. 1193–1211.

Ge, Z., and Han, F., 1986, Marine volcanic hydrothermal sedimentary characteristics of Dabaoshan iron-polymetallic deposit: Mineral Deposits, v. 5, p. 1–12 (in Chinese with English abs.).

Gehrig, M., Lentz, H., and Franck, E.U., 1986, The system water carbondioxide sodium-chloride to 773–K and 300–Mpa: Berichte Der Bunsen-Gesellschaft-Physical Chemistry Chemical Physics, v. 90, p. 525–533.

Gilder, S.A., Gill, J., Coe, R.S., Zhao, X.X., Liu, Z.W., Wang, G.X., Yuan, K.R., Liu, W.L., Kuang, G.D., and Wu, H.R., 1996, Isotopic and paleomagnetic constraints on the Mesozoic tectonic evolution of south China: Journal of Geophysical Research-Solid Earth, v. 101, p. 16,137–16,154.

Goldstein, R.H., 2003, Petrographic analysis of fluid inclusions: Mineralogical Association of Canada, Short Course 32, p. 9–54.

Goldstein, R.H., and Reynolds, T.J., 1994, Systematics of fluid inclusions in diagenetic minerals: Society of Sedimentary Geology, SEPM Short Course 31, 199 p.

Götte, T., Pettke, T., Ramseyer, K., Koch-Müller, M., and Mullis, J., 2011, Cathodoluminescence properties and trace element signature of hydrothermal quartz: A fingerprint of growth dynamics: American Mineralogist, v. 96, p. 802–813.

Götze, J., 2009, Chemistry, textures and physical properties of quartz-geological interpretation and technical application: Mineralogical Magazine, v. 73, p. 645–671.

Götze, J., Plötze, M., and Habermann, D., 2001, Origin, spectral characteristics and practical applications of the cathodoluminescence (CL) of quartz—a review: Mineralogy and Petrology, v. 71, p. 225–250.

Götze, J., Plötze, M., Graupner, T., Hallbauer, D.K., and Bray, C.J., 2004, Trace element incorporation into quartz: A combined study by ICP-MS, electron spin resonance, cathodoluminescence, capillary ion analysis, and gas chromatography: Geochimica et Cosmochimica Acta, v. 68, p. 3741–3759.

Gustafson, L.B., and Hunt, J.P., 1975, The porphyry copper-deposit at El-Salvador, Chile: Economic Geology, v. 70, p. 857–912.

Hedenquist, J.W., Arribas, A., and Reynolds, T.J., 1998, Evolution of an intrusion-centered hydrothermal system: Far Southeast-Lepanto porphyry and epithermal Cu-Au deposits, Philippines: Economic Geology, v. 93, p. 373–404.

Heinrich, C.A., Günther, D., Audétat, A., Ulrich, T., and Frischknecht, R., 1999, Metal fractionation between magmatic brine and vapor, determined by microanalysis of fluid inclusions: Geology, v. 27, p. 755–758.

Hickman, S.H., Barton, C.A., Zoback, M.D. Morin, R., Sass, J., and Benoit, R., 1997, In situ stress and fracture permeability along the Stillwater fault zone Dixie Valley, Nevada: International Journal of Rock Mechanics and Mining Sciences, v. 34, p. 414–423.

Holtz, F., Becker, A., Freise, M., and Johannes, W., 2001, The water-undersaturated and dry Qz-Ab-Or system revisited. Experimental results at very low water activities and geological implications: Contributions to Mineralogy and Petrology, v. 141, p. 347–357.

Hsü, K.J., Li, J., Chen, H., Wang, Q., Sun, S., and Şengör, A.M.C., 1990, Tectonics of South China: Key to understanding West Pacific geology: Tectonophysics, v. 183, p. 9–39.

Huang, R.F., and Audétat, A., 2012, The titanium-in-quartz (TitaniQ) thermobarometer: A critical examination and re-calibration: Geochimica et Cosmochimica Acta, v. 84, p. 75–89.

Huang, S., Zeng, Y., Jia, G., and Chen, Y., 1987, On the genesis of Dabaoshan polymetallic deposit in Guangdong Province, China: Geochimica, v. 1, p. 27–35 (in Chinese with English abs.).

Huenges, E., Erzinger, J., Kuck, J., Engeser, B., and Kessels, W., 1997, The permeable crust: Geohydraulic properties down to 9121 m depth: Journal of Geophysical Research, v. 102, p. 18255–18265.

Jacamon, F., and Larsen, R.B., 2009, Trace element evolution of quartz in the charnockitic Kleivan granite, SW-Norway: The Ge/Ti ratio of quartz as an index of igneous differentiation: Lithos, v. 107, p. 281–291.

Jochum, K.P., Weis, U., Stoll, B., Kuzmin, D., Yang, Q., Raczek, I., Jacob, D.E., Stracke, A., Birbaum, K., Frick, D.A., Günther, D., and Enzweiler, J., 2011, Determination of reference values for NIST SRM 610-617 glasses following ISO guidelines: Geostandards and Geoanalytical Research, v. 35, p. 397–429.

John, D.A., 1989, Geologic setting, depths of emplacement, and regional distribution of fluid inclusions in intrusions of the central Wasatch Mountains, Utah: Economic Geology, v. 84, p. 386–409.

Johnson, J.W., Oelkers, E.H., and Helgeson, H.C., 1992, Supcrt92—a software package for calculating the standard molal thermodynamic properties of minerals, gases, aqueous species, and reactions from 1-bar to 5000-bar and 0-degrees-C to 1000-degrees-C: Computers and Geosciences, v. 18, p. 899–947.

Jourdan, A.L., Vennemann, T.W., Mullis, J., Ramseyer, K., and Spiers, C.J., 2009, Evidence of growth and sector zoning in hydrothermal quartz from Alpine veins: European Journal of Mineralogy, v. 21, p. 219–231.

Klemm, L.M., Pettke, T., Heinrich, C.A., and Campos, E., 2007, Hydrothermal evolution of the El Teniente deposit, Chile: Porphyry Cu-Mo ore deposition from low-salinity magmatic fluids: Economic Geology, v. 102, p. 1021–1045.

Klemm, L.M., Pettke, T., and Heinrich, C.A., 2008, Fluid and source magma evolution of the Questa porphyry Mo deposit, New Mexico, USA: Mineralium Deposita, v. 43, p. 533–552.

Kouzmanov, K., Pettke, T., and Heinrich, C.A., 2010, Direct analysis of ore-precipitating fluids: Combined IR microscopy and LA-ICP-MS study of fluid inclusions in opaque ore minerals: Economic Geology, v. 105, p. 351–373.

Lambrecht, G., and Diamond, L.W., 2014, Morphological ripening of fluid inclusions and coupled zone-refining in quartz crystals revealed by cathodoluminescence imaging: Implications for CL-petrography, fluid inclusion analysis and trace-element geothermometry: Geochimica et Cosmochimica Acta, v. 141, 381–406.

Landtwing, M.R., and Pettke, T., 2005, Relationships between SEM-cathodoluminescence response and trace-element composition of hydrothermal vein quartz: American Mineralogist, v. 90, p. 122–131.

Landtwing, M., Pettke, T., Halter, W., Heinrich, C., Redmond, P., Einaudi, M., and Kunze, K., 2005, Copper deposition during quartz dissolution by cooling magmatic-hydrothermal fluids: The Bingham porphyry: Earth and Planetary Science Letters, v. 235, p. 229–243.

Larsen, R.B., Polvé, M., and Juve, G., 2000, Granite pegmatite quartz from Evje-Iveland: Trace element chemistry and implications for the formation of high-purity quartz: Bulletin Geological Survey Norway, v. 436, p. 57–65.

Larsen, R.B., Henderson, I., Ihlen, P.M., Jacamon, F., 2004, Distribution and petrogenetic behaviour of trace elements in granitic pegmatite quartz from South Norway: Contributions to Mineralogy and Petrology, v. 147, p. 615–628.

Leeman, W.P., Macrae, C.M., Wilson, N.C., Torpy, A., Lee, C.T., Student, J.J., Thomas, J.B., and Vicenzi, E.P., 2012, A study of cathodoluminescence and trace element compositional zoning in natural quartz from volcanic rocks: Mapping titanium content in quartz: Microscopy and Microanalysis, v. 18, p. 1322–1341.

Lehmann, K., Berger, A., Götte, T., Ramseyer, K., and Wiedenbeck, M., 2009, Growth related zonations in authigenic and hydrothermal quartz characterized by SIMS-, EPMA-, SEM-CL- and SEM-CC-imaging: Mineralogical Magazine, v. 73, p. 633–643.

Li, C.Y., Zhang, H., Wang, F.Y., Liu, J.Q., Sun, Y.L., Hao, X.L., Li, Y.L., and Sun, W., 2012, The formation of the Dabaoshan porphyry molybdenum deposit induced by slab rollback: Lithos, v. 150, p. 101–110.

Li, X., Watanabe, Y., Hua, R., and Mao, J., 2008, Mesozoic Cu-(Mo)-W-Sn mineralization and ridge/triple subduction in South China: Acta Geologica Sinica, v. 85, p. 625–640 (in Chinese with English abs.).

Li, Z.X., and Li, X.H., 2007, Formation of the 1300-km-wide intracontinental orogen and postorogenic magmatic province in Mesozoic South China: A flat-slab subduction model: Geology, v. 35, p. 179–182.

Linnen, R.L., and Williams-Jones, A.E., 1990, Evolution of aqueous-carbonic fluids during contact metamorphism, wall-rock alteration, and molybdenite deposition at Trout Lake, British Columbia: Economic Geology, v. 85, p. 1840–1856.

Liu, C.Z., Liu, Z.C., Wu, F.Y., and Chu, Z.Y., 2012, Mesozoic accretion of juvenile sub-continental lithospheric mantle beneath South China and its implications: Geochemical and Re-Os isotopic results from Ningyuan mantle xenoliths: Chemical Geology, v. 291, p. 186–198.

Liu, G., Yang, S., Zhang, X., and Chen, C., 1985, A primary study on the genesis of the Dabaoshan polymetallic deposit in northern Guangdong: Acta Geologica Sinica, v. 1, p. 47–61 (in Chinese with English abs.).

Liu, X., and Zhou, S., 1985, On the occurrence of Middle Ordovician volcanics and analysis of ore-forming mechanism of siderite polymetallic deposit from Dabaoshan, Qujiang County, Guangdong province: Journal of Nanjing University (Natural Sciences Edition), v. 21, p. 348–361 (in Chinese with English abs.).

Lund, B., and Zoback, M.D., 1999, Orientation and magnitude of in situ stress to 6.5 km depth in the Baltic Shield: International Journal of Rock Mechanics and Mining Sciences, v. 36, 169–190.

Manske, S.L., and Paul, A.H., 2002, Geology of a major new porphyry copper center in the Superior (Pioneer) district, Arizona: Economic Geology, v. 97, p. 197–220.

Mao, J., Xie, G., Guo, C., Yuan, S., Cheng, Y., and Chen, Y., 2008, Spatial-temporal distribution of Mesozoic ore deposits in South China and their metallogenic settings: Geological Journal of China Universities, p. 510–526 (in Chinese with English abs.).

Mao, J., Pirajno, F., and Cook, N., 2011, Mesozoic metallogeny in East China and corresponding geodynamic settings—an introduction to the special issue: Ore Geology Reviews, v. 43, p. 1–7.

Mao, W., Li, X., and Yang, F., 2013, Zircon LA-ICP-MS U-Pb ages of granites at Dabaoshan polymetallic deposit and its geological significance, Guangdong, South China: Acta Petrologica Sinica, v. 29, p. 4104–4120 (in Chinese with English abs.).

Martin, J.J., and Armington, A.F., 1983, Effect of growth-rate on quartz defects: Journal of Crystal Growth, v. 62, p. 203–206.

Maydagán, L., Franchini, M., Rusk, B., Lentz, D.R., McFarlane, C., Impiccini, A., Ríos, F.J., and Rey, R., 2015, Porphyry to epithermal transition in the Altar Cu-(Au-Mo) deposit, Argentina, studied by cathodoluminescence, LA-ICP-MS, and fluid inclusion analysis: Economic Geology, v. 110, p. 889–923.

Mercer, C.N., and Reed, M.H., 2013, Porphyry Cu-Mo stockwork formation by dynamic, transient hydrothermal pulses: Mineralogic insights from the deposit at Butte, Montana: Economic Geology, v. 108, p. 1347–1377.

Mercer, C.N., Reed, M.H., and Mercer, C.M., 2015, Time scales of porphyry Cu deposit formation: Insights from titanium diffusion in quartz: Economic Geology, v. 110, p. 587–602.

Müller, A., and Knies, J., 2013, Trace elements and cathodoluminescence of detrital quartz in Arctic marine sediments—a new ice-rafted debris provenance proxy: Climate of the Past, v. 9, p. 2615–2630.

Müller, A., Wiedenbeck, M., van den Kerkhof, A.M., Kronz, A., and Simon, K., 2003, Trace elements in quartz—a combined electron microprobe, secondary ion mass spectrometry, laser-ablation ICP-MS, and cathodoluminescence study: European Journal of Mineralogy, v. 15, p. 747–763.

Müller, A., Wiedenbeck, M., Flem, B., and Schiellerup, H., 2008, Refinement of phosphorus determination in quartz by LA-ICP-MS through defining new reference material values: Geostandards and Geoanalytical Research, v. 32, p. 361–376.

Müller, A., Herrington, R., Armstrong, R., Seltmann, R., Kirwin, D.J., Stenina, N.G., and Kronz, A., 2010, Trace elements and cathodoluminescence of quartz in stockwork veins of Mongolian porphyry-style deposits: Mineralium Deposita, v. 45, p. 707–727.

Müller, A., Wanvik, J.E., and Ihlen, P.M., 2012, Petrological and chemical characterisation of high-purity quartz deposits with examples from Norway, *in* Gotze, J., and Mockel, R., eds., Quartz: deposits, mineralogy and analytics, 1st ed.: Springer Geology, p. 71–118.

Muntean, J.L., and Einaudi, M.T., 2000, Porphyry gold deposits of the Refugio district, Maricunga belt, northern Chile: Economic Geology, v. 95, p. 1445–1472.

——2001, Porphyry-epithermal transition: Maricunga belt, northern Chile: Economic Geology, v. 96, p. 743–772.

Naney, M.T., 1983, Phase equilibria of rock-forming ferromagnesian silicates in granitic systems: American Journal of Science, v. 283, p. 993–1033.

O'Neil, J.R., and Taylor, H.P., Jr., 1969, Oxygen isotope equilibrium between muscovite and water: Journal of Geophysical Research, v. 74, p. 6012–6022.

Penniston-Dorland, S.C., 2001, Illumination of vein quartz textures in a porphyry copper ore deposit using scanned cathodoluminescence: Grasberg Igneous Complex, Irian Jaya, Indonesia: American Mineralogist, v. 86, p. 652–666.

Redmond, P.B., Einaudi, M.T., Inan, E.E., Landtwing, M.R., and Heinrich, C.A., 2004, Copper deposition by fluid cooling in intrusion-centered systems: New insights from the Bingham porphyry ore deposit, Utah: Geology, v. 32, p. 217–220.

Roedder, E., 1984, Fluid inclusions: Reviews in Mineralogy, v. 12, 644 p.

Rusk, B.G., 2006, Intensity of quartz cathodoluminescence and trace-element content in quartz from the porphyry copper deposit at Butte, Montana: American Mineralogist, v. 91, p. 1300–1312.

——2012, Cathodoluminescent textures and trace elements in hydrothermal quartz, *in* Gotze, J., and Mockel, R., eds., Quartz: Deposits, mineralogy and analytics, 1st ed.: Springer Geology, p. 307–329.

Rusk, B., and Reed, M., 2002, Scanning electron microscope-cathodoluminescence analysis of quartz reveals complex growth histories in veins from the Butte porphyry copper deposit, Montana: Geology, v. 30, p. 727–730.

Rusk, B.G., Reed, M.H., and Dilles, J.H., 2008a, Fluid inclusion evidence for magmatic-hydrothermal fluid evolution in the porphyry copper-molybdenum deposit at Butte, Montana: Economic Geology, v. 103, p. 307–334.

Rusk, B.G., Lowers, H.A., and Reed, M.H., 2008b, Trace elements in hydrothermal quartz: Relationships to cathodoluminescent textures and insights into vein formation: Geology, v. 36, p. 547–550.

Seedorff, E., Dilles, J.H., John M. Proffett, J., Einaudi, M.T., Zurcher, L., Stavast, W.J.A., Johnson, D.A., and Barton, M.D., 2005, Porphyry deposits: Characteristics and origin of hypogene features: Economic Geology 100th Anniversary Volume, p. 251–298.

Seedorff, E., Barton, M.D., Stavast, W.J. A., and Maher, D.J., 2008, Root zones of porphyry systems: Extending the porphyry model to depth: Economic Geology, v. 103, p. 939–956.

Selby, D., Nesbitt, B.E., Muehlenbachs, K., and Prochaska, W., 2000, Hydrothermal alteration and fluid chemistry of the Endako porphyry molybdenum deposit, British Columbia: Economic Geology, v. 95, p. 183–202.

Shu, L.S., Zhou, X.M., Deng, P., Yu, X.Q., Wang, B., and Zu, F.P., 2004, Geological features and tectonic evolution of Meso-Cenozoic basins in southeastern China: Geological Bulletin of China, v.23, 876–884 (in Chinese with English abs.).

Shu, X.J., Wang, X.L., Sun, T., Xu, X., and Dai, M.N., 2011, Trace elements, U-Pb ages and Hf isotopes of zircons from Mesozoic granites in the western Nanling Range, South China: Implications for petrogenesis and W-Sn mineralization: Lithos, v. 127, p. 468–482.

Sillitoe, R.H., 2010, Porphyry copper systems: Economic Geology, v. 105, p. 3–41.

Sippel, R.F., 1968, Sandstone petrology, evidence from luminescence petrography: Journal of Sedimentary Research, v. 38, p. 530–554.

Smith, J.V., and Stenstrom, R.C., 1965, Electron-excited luminescence as a petrologic tool: Journal of Geology, v. 73, p. 627–635.

Song, S., Hu, K., Jiang, S., and Li, K., 2007, The He-Ar-Pb-S isotope tracing on ore-forming fluid in Dabaoshan polymetallic deposit, North Guangdong: Contributions to Geology and Mineral Resources Research, v. 22, p. 87–99 (in Chinese with English abs.).

Sun, W., Ding, X., Hu, Y.H., and Li, X.H., 2007, The golden transformation of the Cretaceous plate subduction in the west Pacific: Earth and Planetary Science Letters, v. 262, p. 533–542.

Sun, W.D., Yang, X.Y., Fan, W.M., and Wu, F.Y., 2012, Mesozoic large scale magmatism and mineralization in South China: Preface: Lithos, v. 150, p. 1–5.

Tarantola, A., Diamond, L.W., Stünitz, H., Thust, A., and Pec, M., 2012, Modification of fluid inclusions in quartz by deviatoric stress. III: Influence of principal stresses on inclusion density and orientation: Contributions to Mineralogy and Petrology, v. 164, p. 537–550.

Thomas, J., Watson, E., Spear, F., Shemella, P., Nayak, S., and Lanzirotti, A., 2010, TitaniQ under pressure: The effect of pressure and temperature on the solubility of Ti in quartz: Contributions to Mineralogy and Petrology, v. 160, p. 743–759.

Townend, J., and Zoback, M.D., 2000, How faulting keeps the crust strong: Geology, v. 28, p. 399–402.

Wang, F.Y., Ling, M.X., Ding, X., Hu, Y.H., Zhou, J.B., Yang, X.Y., Liang, H.Y., Fan, W.M., and Sun, W., 2011, Mesozoic large magmatic events and mineralization in SE China: Oblique subduction of the Pacific plate: International Geology Reviews, v. 53, p. 704–726.

Wang, L., Hu, M., Yang, Z., Chen, K., and Xia, J., 2010, Geochronology and its geological implication of LA-ICP-MS zircon U-Pb dating of granodiorite porphyries in Dabaoshan polumetallic ore deposit, North Guangdong province: Earth Science-Journal of China University of Geosciences, v. 35, p. 175–185 (in Chinese with English abs.).

Wang, L., Hu, M., Yang, Z., Qu, W., Xia, J., and Chen, K., 2011, U-Pb and Re-Os geochronology and geodynamic setting of the Dabaoshan polymetallic deposit, northern Guangdong province, South China: Ore Geology Reviews, v. 43, p. 40–49.

Wang, Y., Fan, W., and Guo, F., 2003, Geochemistry of early Mesozoic potassium-rich diorites-granodiorites in southeastern Hunan province, South China: Petrogenesis and tectonic implications: Geochemical Journal, v. 37, p. 427–448.

Wang, Y., Fan, W., Peng, T., and Guo, F., 2004, Elemental and Sr-Nd isotopic systematics of the early Mesozoic volcanic sequence in southern Jiangxi province, South China: Petrogenesis and tectonic implications: International Journal of Earth Sciences, v. 94, p. 53–65.

Wark, D.A., Hildreth, W., Spear, F.S., Cherniak, D.J., and Watson, E.B., 2007, Pre-eruption recharge of the Bishop magma system: Geology, v. 35, p. 235–238.

Watson, E.B., 1996, Surface enrichment and trace-element uptake during crystal growth: Geochimica et Cosmochimica Acta, v. 60, p. 5013–5020.

——2004, A conceptual model for near-surface kinetic controls on the trace-element and stable isotope composition of abiogenic calcite crystals: Geochimica et Cosmochimica Acta, v. 68, p. 1473–1488.

Watson, E.B., and Liang, Y., 1995, A simple model for sector zoning in slowly grown crystals: Implications for growth rate and lattice diffusion, with emphasis on accessory minerals in crustal rocks: American Mineralogist, v. 80, p. 1179–1187.

Wilkins, R.W.T., 1977, Fluid inclusion assemblages of the stratiform Broken Hill ore deposit, New South Wales, Australia: Science, v. 198, p. 185–187.

Wilson, A.J., Cooke, D.R., and Harper, B.L., 2003, The Ridgeway gold-copper deposit: A high-grade alkalic porphyry deposit in the Lachlan fold belt, New South Wales, Australia: Economic Geology, v. 98, p. 1637–1666.

Wu, J., Wang, G.Q., Liang, H.Y., Huang, W.T., Lin, S.P., Zou, Y.Q., Sun, W.D., and Wang, Y.W., 2014, Idenfication of Calidonian volcanic rock in the Dabaoshan ore-filed in northern Guangdong province and its geological implication: Acta Petrologica Sinica, v. 30, p. 1145–1154 (in Chinese with English abs.).

Xu, W., Li, H., Chen, M., Huang, D., Zhang, F., and Wang, L., 2008, Isotope evidence of material sources of the Dabaoshan polymetallic deposit: Acta Geoscientica Sinica, v. 29, p. 684–690 (in Chinese with English abs.).

Yang, Z., 1997, Origin of the Dabaoshan massive sulfide deposit: Devonian sea-floor thermal events: Geology and Mineral Resources of South China, v. 1, p. 7–17 (in Chinese with English abs.).

Yao, D., and Zeng, L., 1994, On genesis of Dabaoshan mineral deposit: Acta Scientiarum Naturalium Universitatis Sunyatseni, v. 33, p. 91–100 (in Chinese with English abs.).

Ye, L., Cook, N.J., Ciobanu, C.L., Yuping, L., Qian, Z., Tiegeng, L., Wei, G., Yulong, Y., and Danyushevskiy, L., 2011, Trace and minor elements in sphalerite from base metal deposits in South China: A LA-ICPMS study: Ore Geology Reviews, v. 39, p. 188–217.

Ye, L., Liu, T., Yang, Y., Gao, W., Pan, Z., and Bao, T., 2014, Petrogenesis of bismuth minerals in the Dabaoshan Pb-Zn polymetallic massive sulfide deposit, northern Guangdong province, China: Journal of Asian Earth Sciences, v. 82, p. 1–9.

Zhou, X.M., and Li, W.X., 2000, Origin of late Mesozoic igneous rocks in southeastern China: Implications for lithosphere subduction and underplating of mafic magmas: Tectonophysics, v. 326, p. 269–287.

Zhou, X.M., Sun, T., Shen, W.Z., Shu, L.S., and Niu, Y.L., 2006, Petrogenesis of Mesozoic granitoids and volcanic rocks in South China: A response to tectonic evolution: Episodes, v. 29, p. 26–33.